



**UNIVERSIDAD NACIONAL AUTÓNOMA DE MÉXICO**  
**PROGRAMA DE POSGRADO EN ASTROFÍSICA**

Instituto de Radioastronomía y Astrofísica

**EL IMPACTO DEL VIENTO ESTELAR Y LA RADIACIÓN  
EN GLÓBULOS NEUTROS ALREDEDOR DE UNA  
ESTRELLA WOLF-RAYET**

**TESIS  
PARA OPTAR POR EL GRADO DE  
MAESTRO EN CIENCIAS (ASTROFÍSICA)**

**PRESENTA:  
ROBERTO REYES CABANAS**

**TUTOR:  
DR. WILLIAM JOHN HENNEY  
Instituto de Radioastronomía y Astrofísica**

Morelia, Michoacán, México, abril 2025



# Abstract

The circumstellar nebula M1-67 around the Wolf–Rayet star WR 124 contains hundreds of small neutral globules, as revealed by recent images from the *James Webb Space Telescope* (JWST). The ionized emission of the nebula displays an intricate pattern of shells and filaments, many of which appear associated with the globules but displaced toward the central star. We propose a simple model for the nebula in which photoevaporative flows from the irradiated surfaces of the globules interact with the stellar wind of the Wolf–Rayet star to form hemispherical emission shells. We test this model against JWST and H $\alpha$  images of the nebula obtained with the *Hubble Space Telescope* (HST), finding good agreement for the best-observed and most isolated globules. The model provides a physical explanation for the observed morphology of the nebula and globules, and suggests that the globules are hydrodynamically shielded from the stellar wind by the photoevaporative flows. We derive an independent estimate of the stellar wind strength, which is consistent with values previously obtained from stellar atmosphere modeling. We are also able to constrain the three-dimensional distribution of the globules.



# Acknowledgements

The person I most wish to thank is my advisor, Dr. Will. He guided me throughout the entire master's program and was always there for me, especially in the most difficult moments. Thanks to him, my adventure in the world of astronomy has been the most wonderful I have ever experienced. Thank you, Doctor, for all the patience, support, and knowledge you shared with me.

I would also like to thank UNAM in general: for accepting me into the graduate program, which for me was quite a challenge; for providing all the facilities I needed to carry out my studies; and for giving me the chance to share them with others. To the Morelia campus, because there I met my dance teacher Lupita and all my dear friends, whom I cherish with all my heart. With you I learned that it is not necessary to look up at the sky to see the stars—especially if it is to watch them dance. To IRyA for giving me its unconditional support, and especially to the outreach team, because although you may not believe it, at your events I was always as excited as the children. To mamá Karin for all her patience and affection. Also to my classmates, who were always there—literally.

I want to thank my committee members for their time, suggestions, and comments. With your help I greatly improved my work. Thanks, Toalá!—since it was your fault that I had so much fun with this project that fascinated me so much.

I am grateful to CONAHCYT for the financial support provided for my studies and research. Also to the PAPIIT project IN109823 of DGAPA for the financial support that made this work possible.

Finally, thank you, Dra. Gloria, for crossing paths with me in this life and showing me how wonderful this universe is.

# Contents

<b>1</b>	<b>Introduction</b>	<b>9</b>
1.1	Ionized photoevaporative flows . . . . .	10
1.2	Wolf–Rayet stars and their winds . . . . .	13
1.3	The nebula M1-67 . . . . .	14
1.3.1	HST observations . . . . .	15
1.3.2	JWST observations . . . . .	15
1.4	Structure of the thesis . . . . .	16
<b>2</b>	<b>Analytical models of photoevaporative flows interacting with an external pressure</b>	<b>19</b>
2.1	Steady hydrodynamic model . . . . .	20
2.2	Equation of state and ionization equilibrium . . . . .	22
2.3	Structure of the photoevaporative flow . . . . .	23
2.4	Conditions for the shocked shell . . . . .	25
<b>3</b>	<b>Globules in the M1-67 nebula</b>	<b>29</b>
3.1	Estimating the RAM pressure of the stellar wind . . . . .	31
<b>4</b>	<b>Model fitting to brightness profiles</b>	<b>35</b>
4.1	Measuring the radius in the neutral component . . . . .	38
4.2	Observational errors . . . . .	38
4.2.1	Uncertainties in $r_{\text{shell}}$ and $\mathbf{H}_s$ . . . . .	39
4.2.2	Uncertainty in $r_0$ . . . . .	39
4.2.3	Uncertainties in $B_s$ and $B_0$ . . . . .	40
4.3	Estimating the ionized gas density from H $\alpha$ surface brightness . . . . .	42
4.3.1	Using EM from the observations . . . . .	43
4.4	Good fits . . . . .	43
4.5	Recovered fits . . . . .	44
4.6	Discarded globules . . . . .	45
<b>5</b>	<b>Pressure balance in the shells</b>	<b>49</b>
5.1	Internal pressure balance . . . . .	49
5.2	External pressure balance . . . . .	50
<b>6</b>	<b>Discussion</b>	<b>57</b>

<b>CONTENTS</b>	<b>7</b>
6.1 Identification of globules and their shells . . . . .	57
6.2 Mass of the globules . . . . .	58
6.3 Three-dimensional distribution of the globules . . . . .	59
<b>7 Conclusions</b>	<b>63</b>
<b>A Filtros de las observaciones</b>	<b>65</b>
A.1 Filtro del HST . . . . .	65
A.2 Filtros del JWST . . . . .	65
<b>B Estimación de fuerzas en el flujo fotoevaporativo ionizado</b>	<b>69</b>
B.1 Fuerzas de gravedad . . . . .	71
B.2 Presión de radiación . . . . .	71
<b>C Predicciones del modelo fotoevaporativo para la densidad ionizada en el frente de ionización</b>	<b>73</b>
<b>D Combos de filtros</b>	<b>75</b>
<b>E Errores en <math>r_{\text{shell}}</math> y <math>H_s</math></b>	<b>77</b>
<b>F Constante de conversión en las observaciones del HST</b>	<b>79</b>
<b>G Corrección en la estimación de los brillos</b>	<b>81</b>
<b>H Escalas de tiempo</b>	<b>83</b>
H.1 Tiempo dinámico . . . . .	83
H.2 Tiempo de recombinación . . . . .	83
H.3 Tiempo de vida de los glóbulos . . . . .	84
H.3.1 Comparación de las diferentes escalas de tiempo . . . . .	84
<b>I Proyección de posición y velocidad</b>	<b>85</b>
<b>J Imágenes de ajustes</b>	<b>89</b>



# Chapter 1

## Introduction

*Globules* are dense concentrations of gas and dust in the interstellar medium that are thought to form through thermal instabilities, gravitational collapse, or turbulence (Ballesteros-Paredes et al., 2011; Padoan & Nordlund, 2002). These globules can arise in regions of massive star formation or in nebulae around evolved stars, such as planetary nebulae (O'Dell et al., 2007).

In general, globules show a wide range of sizes. For example, when we refer to globules in regions of massive star formation, they are commonly large,  $\sim 0.1$  pc (Schneider et al., 2016), whereas in nebulae around evolved stars they are smaller,  $\sim 10^{-2}$  pc (Gahm et al., 2013).

The first globules were observed by Bart Bok in 1940. As we can see in Figure 1.1, because the background stars are reddened by dust, these globules appear as dark clouds, given their large amounts of neutral gas and dust. The globules contain primarily molecular hydrogen in their interiors, and may also harbor other molecules (Amin & El-Nawawy, 2005; Di Francesco et al., 2002). Although star formation can occur inside them, the ionizing radiation from such stars cannot be observed because it is absorbed by the neutral hydrogen (both molecular and atomic) and the dust between the stars and the observer. For this reason, they appear dark.

When globules are found in regions of massive star formation, they can interact with the ultraviolet (UV) radiation from nearby young massive stars, or with the radiation of the central star if the globules are in a circumstellar nebula. In such cases the ionization front can be seen as a bright rim of emission (see Figures 1.2 and 1.3).

This interaction between stars and globules can occur on different scales, giving rise to a wide variety of structures. Among the largest are those that resemble columns, pillars, or “elephant trunks,” as they are known in the literature. These can reach sizes of  $\sim 1$  pc and densities of order  $10^3 \text{ cm}^{-3}$ . Such interactions can also occur within H II regions, as shown in Figure 1.2.

On smaller scales are the so-called EGGs (Evaporating Gaseous Globules), which have sizes of  $\sim 10^{-2}$  pc, and the proplyds, which are  $\leq 10^{-2}$  pc. These globules are found not only in star forming regions, but also in nebulae around

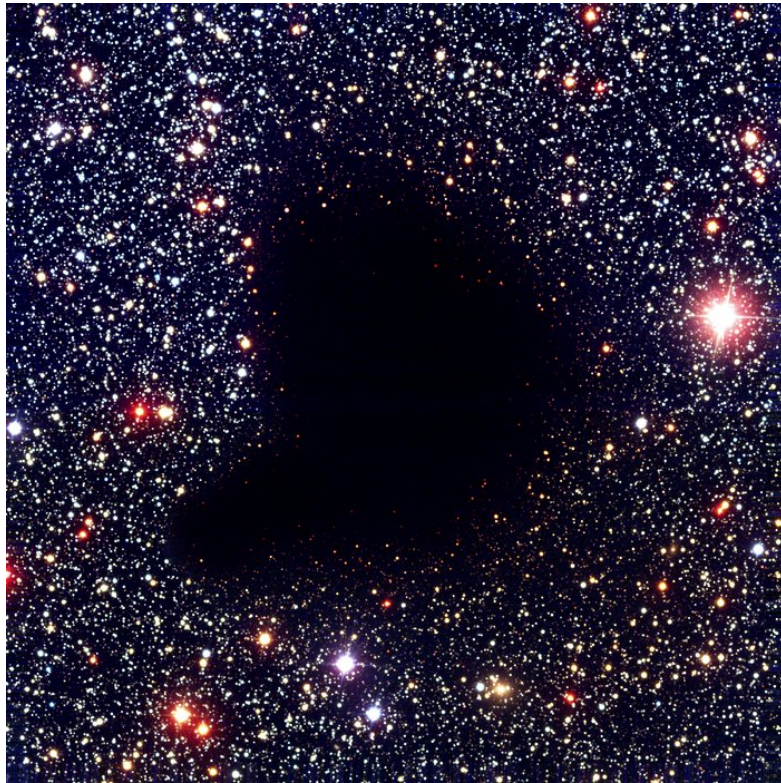


Figure 1.1: Example of a Bok globule. Image of Barnard 68 taken with the Very Large Telescope FORS1 at 440 nm, 557 nm, and 768 nm, with an angular size of  $6.83' \times 6.83'$ . A dark region can be seen, which is the globule itself, together with the apparent reddening of stars caused by dust on the globule's surface. In this image there is no evidence of external photoevaporation from nearby stars (Alves et al., 2001).

evolved stars, where they are more commonly known as *knots*. An example of this is panel **D** in Figure 1.3. In this work we will study in greater detail the knots present in a nebula surrounding a particular evolved star.

## 1.1 Ionized photoevaporative flows

All the examples in Figures 1.1, 1.2, and 1.3 occur either in regions of star formation or in nebulae around evolved stars. What is interesting in all these cases is the way they interact with the most massive stars in their vicinity, for globules found in star-forming regions, or with the evolved central star in planetary nebulae. During these interactions, in some cases we can see what are known as *photoevaporative flows*, which we explain in more detail below.

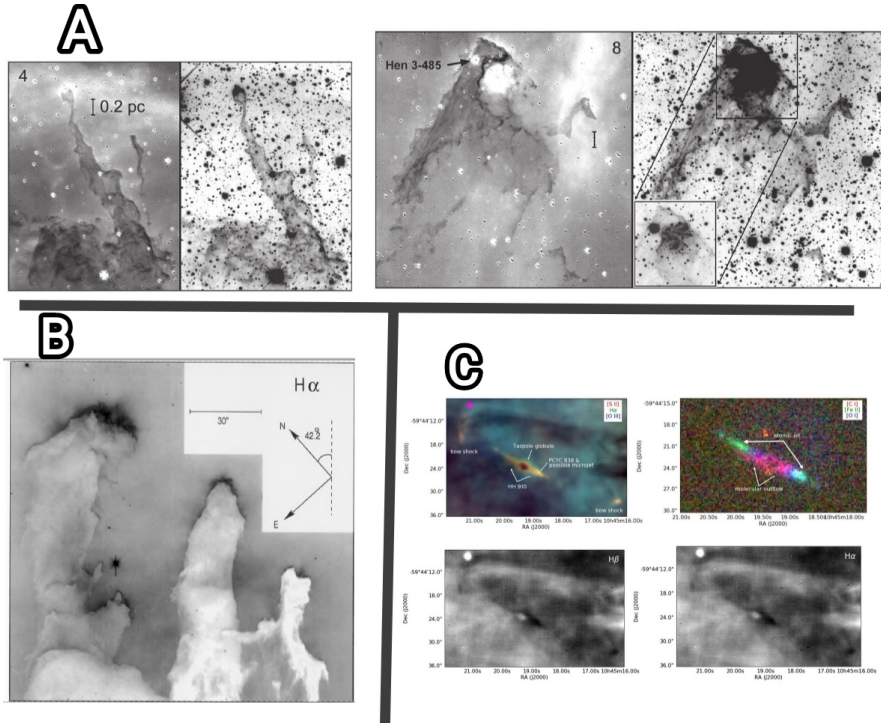


Figure 1.2: **A:** Two examples of pillars. In each case, the right-hand image is observed at  $2.12\text{ }\mu\text{m}$  ( $\text{H}_2$ ) and the left-hand image shows  $\text{H}_2-\text{Br}_\gamma$  (Hartigan et al., 2015). **B:** An example of an elephant trunk. This is an image of M16 taken with WFPC2 using the F656N filter; the  $30''$  bar corresponds to  $9 \times 10^{17}\text{ cm}$  ( $0.29\text{ pc}$ ) (Hester et al., 1996). **C:** The outflow of the Tadpole globule, consisting of the HH900 jet+outflow system. The lower panel shows the object in  $\text{H}\alpha$  with the continuum (Reiter et al., 2019).

When ionizing radiation strikes the surface of a globule, it begins to ionize the neutral gas. The resulting flow of ionized gas that streams away from the base of the globule and travels toward the ionizing source is known as a photoevaporative flow.

In the case of star-forming regions, we can consider a massive star and a dense cloud of neutral gas. In order to observe a photoevaporative flow, the star must be massive, or must have a large ionizing flux capable of ionizing the neutral gas. Otherwise, the photoevaporative flow will not be visible. Recall that in star-forming regions there are many new low-mass stars that emit mainly in radio or infrared, so not all young stars are capable of ionizing the neutral gas.

Oort & Spitzer (1955) give a detailed explanation of the interaction between an O-type star and a cloud of neutral interstellar gas, as observed in regions of

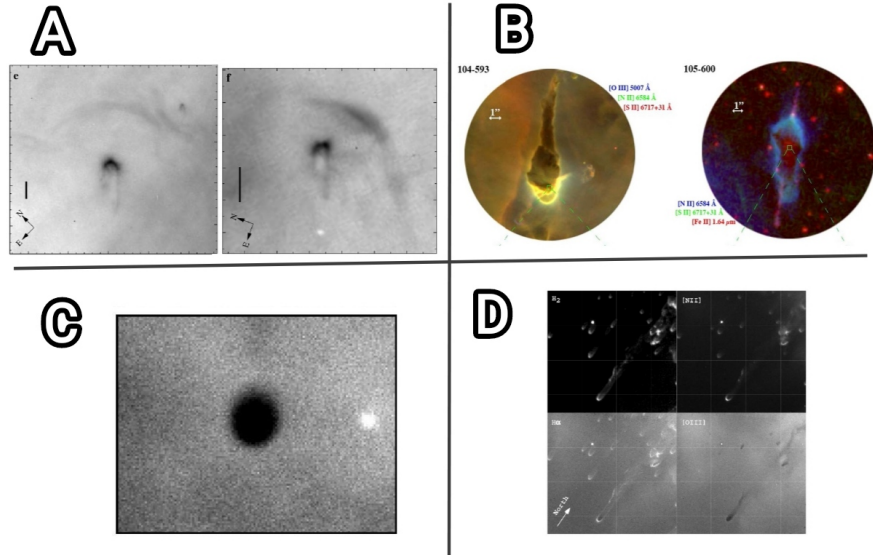


Figure 1.3: **A:** Proplyds with their bow shocks in Orion, observed with the HST Planetary Camera. The black bar indicates a length of  $1''$ , corresponding to  $430 \text{ AU}$  ( $2 \times 10^{-3} \text{ pc}$ ) (García-Arredondo et al., 2001). **B:** Examples of EGGs in Carina, observed with WFC3, ACS, and WFPC2. The white bars of  $1''$  correspond to a physical size of  $10^{-2} \text{ pc}$  (Mesa-Delgado et al., 2016). **C:** The dense globulette RN88 seen in  $\text{H}\alpha$  with a diameter of  $6''$  ( $4 \times 10^{-2} \text{ pc}$ ) in the Rosette Nebula (Gahm et al., 2013). **D:** Examples of knots in the Helix Nebula. The mosaics cover  $47.5'' \times 44.8''$  ( $4.76 \times 10^{-2} \text{ pc} \times 4.49 \times 10^{-2} \text{ pc}$ ) (O'Dell et al., 2007).

massive star formation. They consider three key elements: the ionizing star, the neutral interstellar cloud, and the region between the star and the cloud. The interstellar cloud must be much denser and colder than the intervening region, as shown in Figure 1.4.

When UV radiation begins to heat the gas in the cloud, the ionized gas expands toward the star, since in that direction the density is lower than in the cloud and the gas can expand freely (see Figure 1.5).

At first this radiation ionizes the neutral gas of the cloud at a very rapid rate. As a result, a large number of ionized particles, coming from the cloud, flow toward the star. As the process evolves, an insulating layer forms around the cloud (Oort & Spitzer, 1955). This insulating layer is composed of ionized gas and can protect the cloud from external flows or winds, as well as from radiation.

During this interaction there are both an ionization front and an internal shock that travel through the cloud toward the rear (see Figure 1.5). Initially, these two have a similar velocity of  $\sim 10 \text{ km s}^{-1}$ , but once recombinations in the insulating layer become important, the ionization front begins to decelerate.

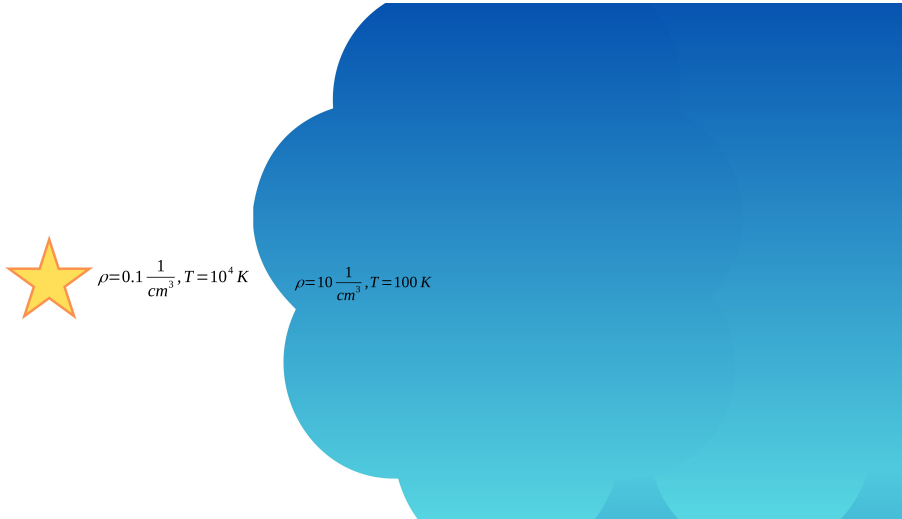


Figure 1.4: Initial schematic used in Oort & Spitzer (1955), in which the cloud is colder and denser than the region between the cloud and the star.

Meanwhile, the internal shock compresses the cloud (Bertoldi, 1989).

It is not always possible to observe a photoevaporative flow from clouds in this type of interaction. For this, Bertoldi (1989) note that if the ionization parameter, defined as

$$\Gamma \equiv \frac{F_i}{n_0 c} \quad (1.1)$$

where  $F_i$  is the incident flux of Lyman continuum photons,  $n_0$  is the density of neutral gas, and  $c$  is the speed of light, is less than  $10^{-7}$ , then the incident ionizing radiation will have no dynamical effect on the cloud, and no photoevaporative flow will be produced. On the other hand, if

$$\delta' \equiv \frac{F_i}{2\alpha_i r_0 n_0^2} > 1 \quad (1.2)$$

where  $\alpha_i$  is the recombination coefficient to all states except the ground state, and  $r_0$  is the radius of the cloud, then the cloud will be completely ionized, since the ionizing flux is greater than the recombinations.

## 1.2 Wolf-Rayet stars and their winds

Wolf-Rayet (WR) stars are the evolved descendants of massive stars, such as O-type stars. These WR stars typically have masses of  $10-25 M_\odot$  and are characterized by intense emission lines and free-free emission at IR-mm-cm wavelengths (Crowther, 2007). They also have high mass-loss rates,  $\sim 2-10 \times 10^{-5} M_\odot/\text{yr}$ , driven by their strong stellar winds, which can reach velocities of  $\sim 1000 \text{ km/s}$ , producing their broad emission lines (Hamann et al., 2006).

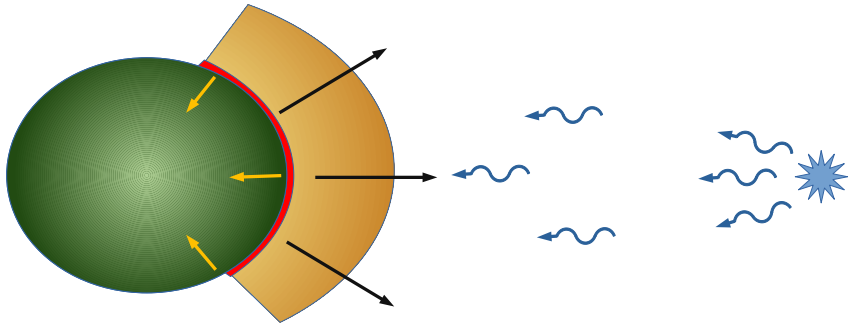


Figure 1.5: Schematic of the initial implosion. When ionizing radiation (blue arrows) strikes the globule (green), it causes ionized gas (orange) to flow toward the star, as shown by the black arrows. In this phase an internal shock is produced that compresses the cloud. Both the shock and the ionization front (red) travel toward the center of the globule, as indicated by the yellow arrows.

They were named after Charles Wolf and Georges Rayet, who first identified three stars in Cygnus with broad emission lines of C, N, O, and He—the characteristic features of this class (Murdin, 2000).

These stars are classified according to the relative strengths of their characteristic emission lines. van der Hucht (2001) classify them mainly as type WN when He and N are abundant, type WC when He and C dominate, and type WO when He and O are abundant. Although many of these stars show no hydrogen in their atmospheres, in some cases a significant amount of H is detected, in which case the designation “h” is added (Smith et al., 1996).

### 1.3 The nebula M1-67

M1-67 is the circumstellar nebula around the WR 124 star, which is of type WN8h. Several studies have been carried out on the M1-67 nebula, including three-dimensional models of its structure based on long-slit spectroscopy (Zavala et al., 2022). Sévigny et al. (2021) used the  $[\text{SII}]\lambda 6717$  and  $\lambda 6731$  lines to find that the electron density decreases with radius: close to the star the electron density is  $\sim 2000 \text{ cm}^{-3}$ , while farther away, at about  $40''$  (1.05 pc), it drops to  $\sim 500 \text{ cm}^{-3}$ . Grosdidier et al. (1998) found that the  $\text{H}\alpha$  surface brightness also decreases with radius as  $r^{-0.8}$ . Marchenko et al. (2010) measured an expansion velocity of  $46 \text{ km s}^{-1}$  for the nebula using observations from 1997 (Grosdidier et al., 1998) and 2008, consistent with the measurement of Zavala et al. (2022).

Figures 1.6 and 1.7 show that this nebula has a very complex structure. Grosdidier et al. (1998) detected some very bright and dense knots, but their nature was not clear. In Chapter 3 we will discuss in detail how these bright and

dense points are in fact globules located throughout much of the nebula. These globules were revealed thanks to images from the James Webb Space Telescope (JWST), which has higher resolution than the Hubble Space Telescope (HST), and also offers a much greater variety of filters.

Throughout this thesis we will use the data in Table 1.1. With the distance to the star,  $D$ , we can derive physical distances as

$$\left[ \frac{R}{\text{AU}} \right] = \left[ \frac{D}{\text{pc}} \right] \left[ \frac{\theta}{\text{arcsec}} \right] \quad (1.3)$$

where  $R$  is the desired physical distance and  $\theta$  is the separation measured directly from the observations in arcseconds. The mass-loss rate,  $\dot{M}$ , and the terminal velocity of the stellar wind,  $v_\infty$ , allow us to calculate the hydrodynamic (RAM) pressure of the stellar wind, while the rate of ionizing photons from the star is used to calculate the radiation pressure.

Parameters of WR 124		
$D$	$5.429 \pm 0.54$ kpc	J. Arthur, priv. comm.
$v_\infty$	710 km/s	Hamann et al. (2006)
$\dot{M}$	$10^{-4.7} M_\odot/\text{yr}$	Crowther et al. (1999)
$S_*$	$1.25 \times 10^{49} \text{ s}^{-1}$	Crowther (2007)

Table 1.1: Parameters of WR 124.

### 1.3.1 HST observations

For the Hubble Space Telescope (HST) observations we used data from the Hubble Legacy Archive. These are FITS images at calibration level 3, meaning they are mosaics created by combining multiple images to cover a region of the sky<sup>1</sup>. We used the F656N filter<sup>2</sup> with the Wide Field and Planetary Camera 2 (WFPC2) to observe H $\alpha$  emission. We used the 1997 data from proposal ID 6787, with a total exposure time of 10 216 s from a combination of 10 exposures. The 2008 data from proposal ID 11137 have a total exposure time of 4200 s from a combination of 8 exposures.

### 1.3.2 JWST observations

For the James Webb Space Telescope (JWST) observations we used data obtained by Klaus M. Pontoppidan, proposal ID 2730. We used the NIRCam filters F090W, F150W, F210M, F335M, F444W, and F470N<sup>3</sup>, with a total exposure time of 2662.72 s. These are level 3 images—mosaics combining multiple exposures to cover a region of the sky—in FITS format.

<sup>1</sup>For more details see [https://hla.stsci.edu/hla\\_faq.html#productlevels](https://hla.stsci.edu/hla_faq.html#productlevels)

<sup>2</sup>Appendix A shows the range covered by this filter.

<sup>3</sup>Appendix A shows the wavelength range of each of these filters.

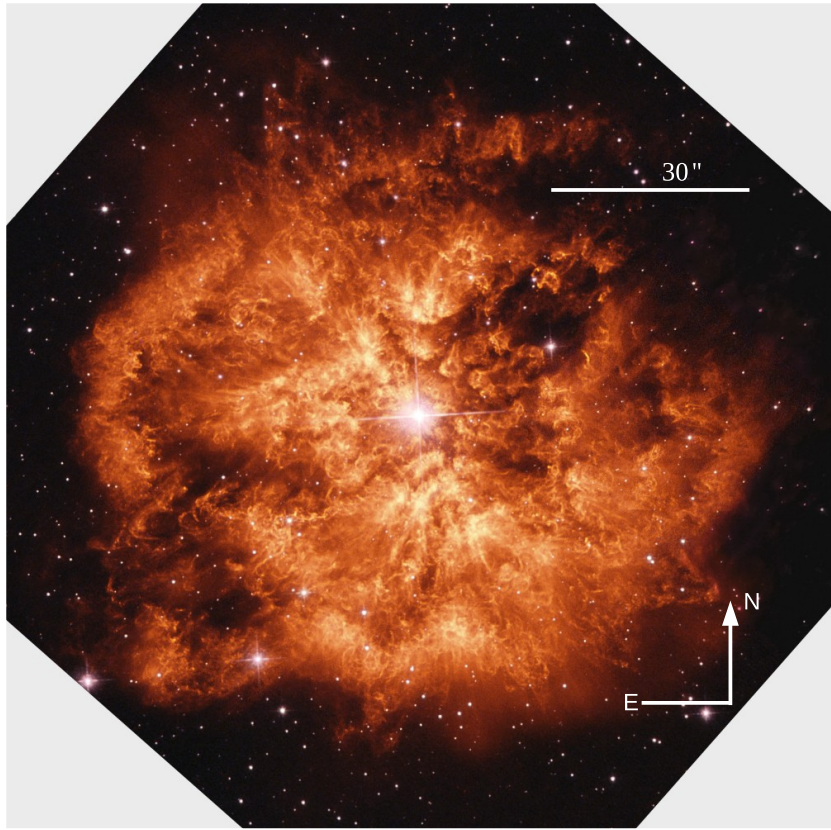


Figure 1.6: Image of M1-67 in the  $\text{H}\alpha$  filter (Grosdidier et al., 1998). The  $30''$  scale corresponds to 0.78 pc. <https://esawebb.org/images/weic2307f/>. The image has been rotated so that North is up and East is to the left.

The wide variety of JWST filters allows us to combine them to observe different emission mechanisms, and its high resolution makes it possible to resolve the detailed structures.

Unlike the  $\text{H}\alpha$  image, the JWST observations use broad-band filters. These bands include contributions from different emission mechanisms: stellar continuum, some nebular emission lines, continuum scattered by dust, thermal dust emission, and also emission from polycyclic aromatic hydrocarbon (PAH) bands.

## 1.4 Structure of the thesis

In this thesis we propose a simple model to explain how the transonic photo-evaporative flow from a globule interacts with an external pressure. We will apply this model to the knots in the M1-67 nebula, and describe how the photo-evaporative flow interacts with the hydrodynamic (RAM) pressure of the stellar

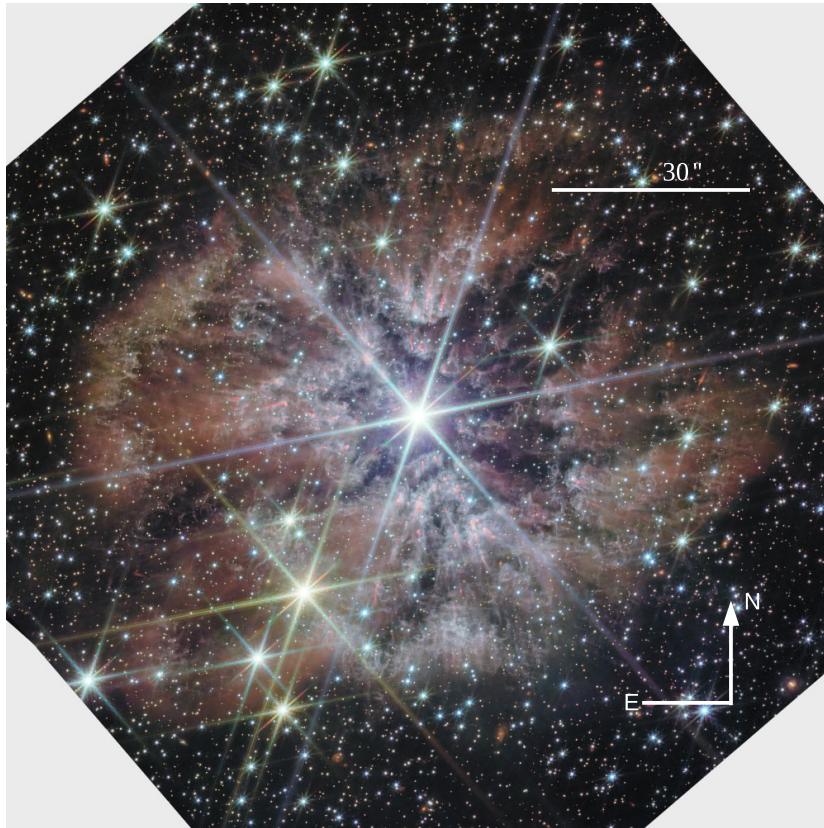


Figure 1.7: Image of M1-67 with JWST. Composite of filters f444w (gray), f335m (red), f210m (green), f150w (turquoise green), and f090w (blue). The  $30''$  scale corresponds to 0.78 pc. <https://www.flickr.com/photos/geckzilla/52757287572/>. The image has been rotated so that North is up and East is to the left.

wind of WR 124.

In Chapter 2 we will see how the interaction between two supersonic flows creates a thin shocked shell. Based on this, we describe a steady-state hydrodynamic model in which the photoevaporative flow of a globule interacts with an external pressure. In this interaction a shocked shell can also be seen.

In Chapter 3 we will describe how we identified the knots in the M1-67 nebula, as well as observational evidence of the interaction between the photoevaporative flow of the knots and the stellar wind of WR 124.

In Chapter 4 we will apply this model to the knots found in the nebula. We will fit the radial brightness profiles in order to measure the knots and their shocked shells. In addition, we can derive the density of the ionized gas from the emission measure.

In Chapter 5 we will compare these results with the theoretical values predicted by the proposed model. This comparison provides a clearer understanding of the distribution of the knots in the nebula.

## Chapter 2

# Analytical models of photoevaporative flows interacting with an external pressure

In this chapter we describe the model proposed to explain the interaction between the photoevaporative flow from a globule and an external pressure. This external pressure can be exerted by the very same star that is photoevaporating the globule. In principle, the model can be applied to any kind of globule like those mentioned in Chapter 1.

In this work we focus on the interaction between the globules' photoevaporative flow<sup>1</sup> in the M1-67 nebula and the RAM pressure of the stellar wind from the star WR 124. In Chapter 3 we will discuss in more detail how we identified these globules in the M1-67 nebula; for now, we concentrate solely on the model.

For this purpose, we assume that all the phases described in Section 1.1 have already taken place and that the system is now in ionization equilibrium. For simplicity, the globule is taken to be spherical in this model.

In the interaction between the (supersonic) photoevaporative flow and the stellar wind, two shocked zones are produced, with a contact discontinuity between them, as depicted in Figure 2.1. Of these zones, we expect to observe only the shocked photoevaporative flow and not the shocked stellar wind, since the latter is less dense, non-radiative, and has a cooling length (zone 3) larger than the interaction region (zone 2).

Cantó et al. (1996) treat in greater detail the interaction between two hypersonic flows produced by two sources separated by a distance  $D$ . In their analysis they assume that a thin shell forms when these two flows reach pressure equilibrium, as shown in Figure 2.2. In our case we likewise expect zone 2

---

<sup>1</sup>For simplicity we will refer to the knots in the nebula as globules.

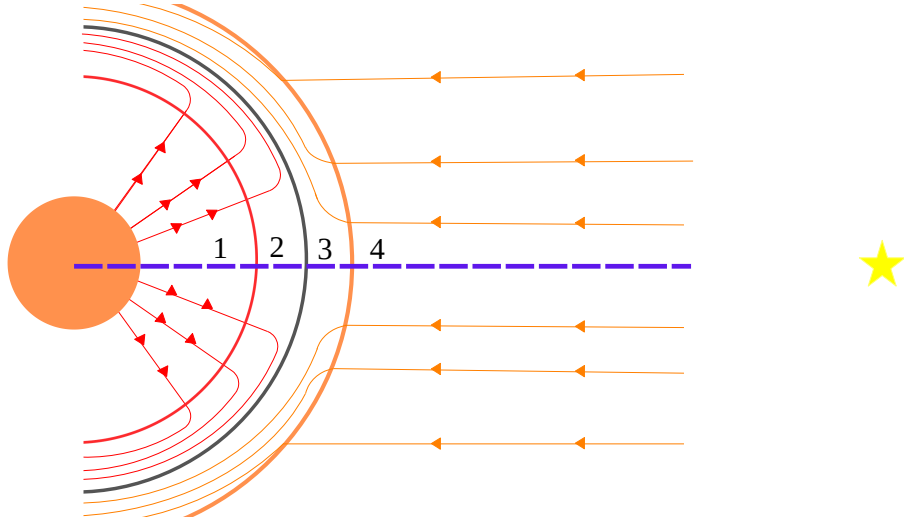


Figure 2.1: The interaction between the photoevaporative flow and the stellar wind of a star forms four zones. The orange circle is the globule. The blue dashed line joining the center of the globule to the center of the star is the symmetry axis adopted in the model; the star lies at the opposite end of the dashed line. Along this symmetry axis both the stellar wind (orange lines) and the radiation strike the base of the globule perpendicularly, while the photoevaporative flow (red lines) travels in the opposite direction. Zone 1 is where the photoevaporative flow emerges from the surface of the globule with Mach number equal to 1 and then increases. Zone 2 is the photoevaporative flow shocked by the stellar wind, which we expect to observe as a shell and to which we refer as the shocked shell. Zone 3 is the stellar wind shocked by the photoevaporative flow, and zone 4 is where the supersonic stellar wind travels, which is less dense than the photoevaporative flow. The contact discontinuity lies between zones 2 and 3 (gray line).

of Figure 2.1 to be thin (Henney & Arthur, 2019).

## 2.1 Steady hydrodynamic model

For our model it is important to note that we do not consider any gravitational force from the star or from the globule itself, nor any other external force (see Appendix B). We assume that only the globule is dominated by a magnetic field, while for the ionized gas we neglect magnetic fields.

In this work we consider as the only external pressure the RAM pressure of the stellar wind from WR 124. Given that the timescale for the phases mentioned in Section 1.1 is very short compared to the interaction timescale between the photoevaporative flow and the stellar wind, we assume that the

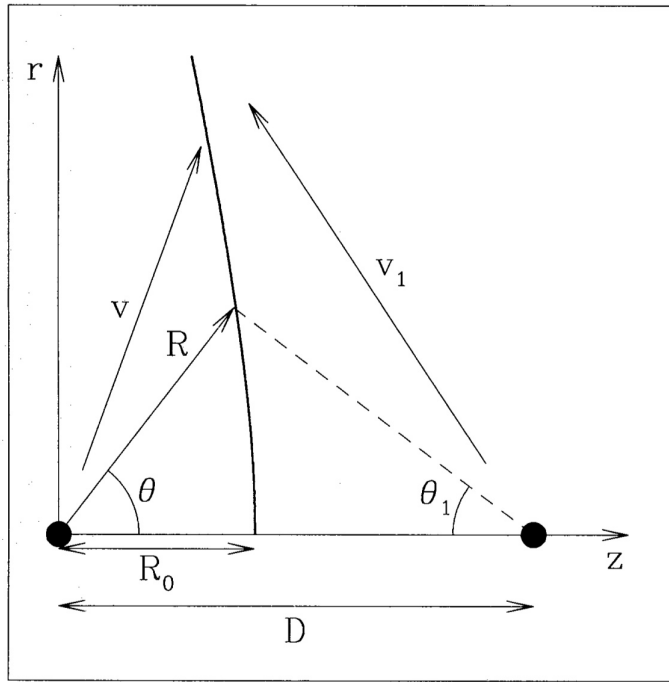


Figure 2.2: Interaction of two supersonic flows produced by two sources (black points on the  $z$  axis) separated by a distance  $D$ . A thin shell  $R(\theta)$  forms in this interaction when the flows reach equilibrium. Cylindrical symmetry is assumed for this problem (Cantó et al., 1996).

insulating layer produced by the UV radiation has already formed and that the system is now in ionization equilibrium. We therefore treat the model as steady: the sizes of the globule and of the shocked shell are taken as constant, since they will not change significantly.

Figure 2.3 shows that we can simplify the problem by placing a small-radius cylinder around the symmetry axis. Within this cylinder we can ignore transverse motions, since gradients in those directions are much smaller than the axial gradients. Near the symmetry axis both the UV radiation and the stellar wind strike the base of the globule perpendicularly, while the photoevaporative flow from the globule travels in the opposite direction. We therefore first solve the problem *on the symmetry axis only*, where it becomes one-dimensional. We then consider how the solution changes at an angle  $\theta$  with respect to the symmetry axis.

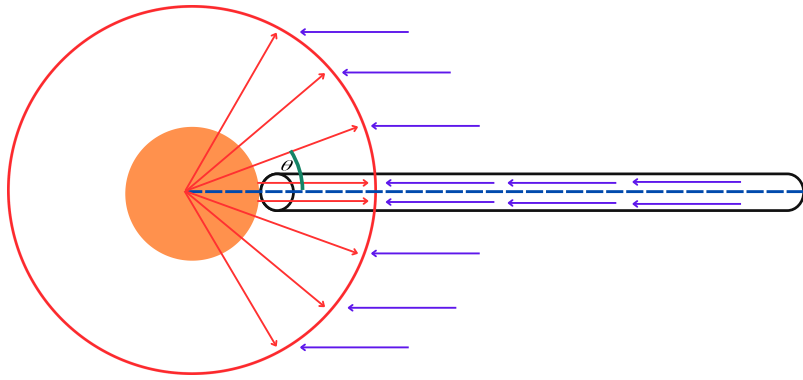


Figure 2.3: Radiation and stellar wind travel toward the globule as indicated by the blue arrows and strike the surface of the globule perpendicularly along the symmetry axis. The photoevaporative flow from the globule travels as shown by the red arrows; therefore, away from the symmetry axis the interaction between this photoevaporative flow and the stellar wind must be considered at a finite angle.

## 2.2 Equation of state and ionization equilibrium

In this case we take the gas interacting with the stellar wind to be an ideal gas, so that our equation of state is

$$PV = Nk_B T, \quad (2.1)$$

where  $P$  is the gas pressure,  $V$  its volume,  $N$  the number of particles,  $k_B$  Boltzmann's constant, and  $T$  the temperature. From this we have

$$P = nk_B T = \frac{\rho k_B T}{\bar{m}} \quad (2.2)$$

where  $n$  is the number density,  $\rho$  the mass density, and  $\bar{m}$  the mean particle mass in the gas. Here we assume the gas is composed mainly of hydrogen, 90% of the total, with a small fraction of helium, so we adopt a mean mass  $\bar{m} = \frac{0.9m_p + 0.1 \times 4m_p}{2} \approx 0.6m_p$  in the ionized gas.

For this ideal gas we take the isothermal sound speed,

$$c_s = \sqrt{\frac{k_B T}{\bar{m}}}, \quad (2.3)$$

so the sound speed in the ionized gas depends only on its temperature. In such gases the sound speed is typically of order  $10^6 \text{ cm s}^{-1}$ .

Since all the phases mentioned in Section 1.1 have already occurred, we assume that the incident flux of ionizing photons,  $F_0$ , is in equilibrium with the recombinations per unit area,

$$F_0 = n_e n_i h_1 \alpha_B, \quad (2.4)$$

where  $h_1$  is the effective thickness and  $\alpha_B$  is the case-B recombination coefficient (see Appendix C). This case-B recombination coefficient accounts for recombinations to all levels except the ground state, since the photon emitted in such a recombination can reionize a nearby atom (Dyson & Williams, 1980).

## 2.3 Structure of the photoevaporative flow

In this model we consider a D-critical ionization front (Shu, 1992); that is, inside the globule there is a subsonic expansion of the gas as seen from the ionization front, while in the ionized gas there is a supersonic expansion as seen from the ionization front. Consequently there is a sonic point located just behind the ionization front. For simplicity we treat the ionization front as a discontinuity across which the gas jumps from neutral to fully ionized, and we therefore take the sonic point to occur exactly at  $r_0$ , the radius of the globule (see Figure 2.4). Thus we assume the gas has Mach number equal to 1 at  $r_0$ , increasing as it traverses zone 1 of Figure 2.1 owing to free expansion. In principle the globule radius and the density at its surface could be taken as free parameters, but with the observations we can measure the radius, and the density can be computed because it must be consistent with our assumption of ionization equilibrium.

With this model we aim to determine where pressure balance is attained between the pressure of the photoevaporative flow and the stellar-wind RAM pressure. For the photoevaporative-flow pressure we include both thermal and hydrodynamic terms, so that the total pressure at the base of the globule is

$$P_{\text{tot}} = P_{\text{ter}} + P_{\text{hid}} = n \bar{m} c_s^2 + n \bar{m} u^2 = \rho c_s^2 (1 + M^2), \quad (2.5)$$

where  $u$  is the velocity of the ionized gas and  $M$  is the Mach number.

This pressure equilibrium is reached at a radius  $r_{\text{shell}}$ , where the pressure of the photoevaporative flow has dropped to a fraction  $f$  of its initial value. Hence the pressure varies as

$$f = \frac{P}{P_0} = \frac{\rho c_s^2 (1 + M^2)}{\rho_0 c_s^2 (1 + 1)} = \frac{\rho}{\rho_0} \frac{1 + M^2}{2}, \quad (2.6)$$

where  $P_0$  is the pressure at the base of the globule. Recall that we are taking the sonic point there, so  $M_0 = 1$ .  $P$  is the pressure of the photoevaporative flow just upstream of  $r_{\text{shell}}$ . From mass conservation we have

$$\rho r^2 M = \rho_0 r_0^2. \quad (2.7)$$

Finally, adopting the isothermal Bernoulli equation,

$$\frac{v^2}{2} + c_s^2 \ln \rho = \text{constant}, \quad (2.8)$$

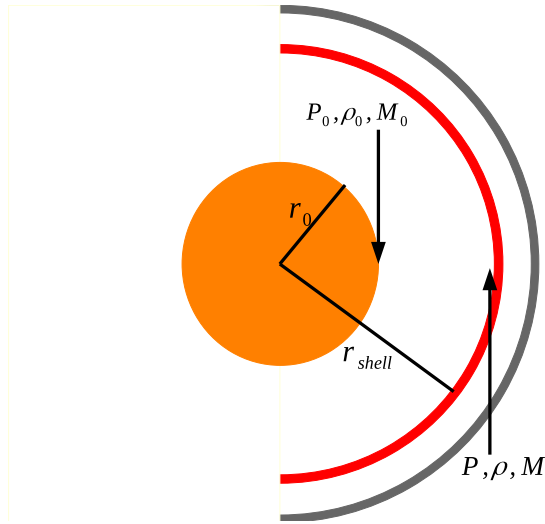


Figure 2.4: In this schematic,  $r_0$  is the radius of the neutral globule, while  $\rho_0$ ,  $M_0$ , and  $P_0$  are the values at the globule surface, varying toward the star until they take on different values at  $r_{\text{shell}}$ , the distance from the globule center to the base of the shocked photoevaporative flow. The quantities  $\rho$ ,  $M$ , and  $P$  are the corresponding values at the base of the shocked photoevaporative flow.

equation (2.5) yields (Dyson, 1968)

$$\frac{r}{r_0} = M^{-1/2} e^{\frac{M^2 - 1}{4}}. \quad (2.9)$$

Combining equations (2.6), (2.7), and (2.9) we obtain

$$f = \frac{1 + M^2}{2} \exp\left(\frac{1 - M^2}{2}\right), \quad (2.10)$$

which depends only on  $M$  and can be solved numerically<sup>2</sup> for different values of  $f$ . Once this equation is solved, the unknowns  $\rho/\rho_0$  and  $r/r_0$  can be obtained from equations (2.7) and (2.9). In this way we find that both the pressure and the density decrease with radius, while the Mach number increases, as shown in Figure 2.5. Note that Figure 2.5 is obtained by solving equations (2.6), (2.7), and (2.9) on the symmetry axis. This would change if we consider a finite angle  $\theta \neq 0$ , since both the pressure and the density scale with angle as  $\cos^{1/2} \theta$ , whereas  $M$  does not (Tarango-Yong & Henney, 2018).

---

<sup>2</sup>In our case we use the function `fsolve` from `scipy.optimize`; see the documentation at <https://docs.scipy.org/doc/scipy-1.12.0/reference/generated/scipy.optimize.fsolve.html>.

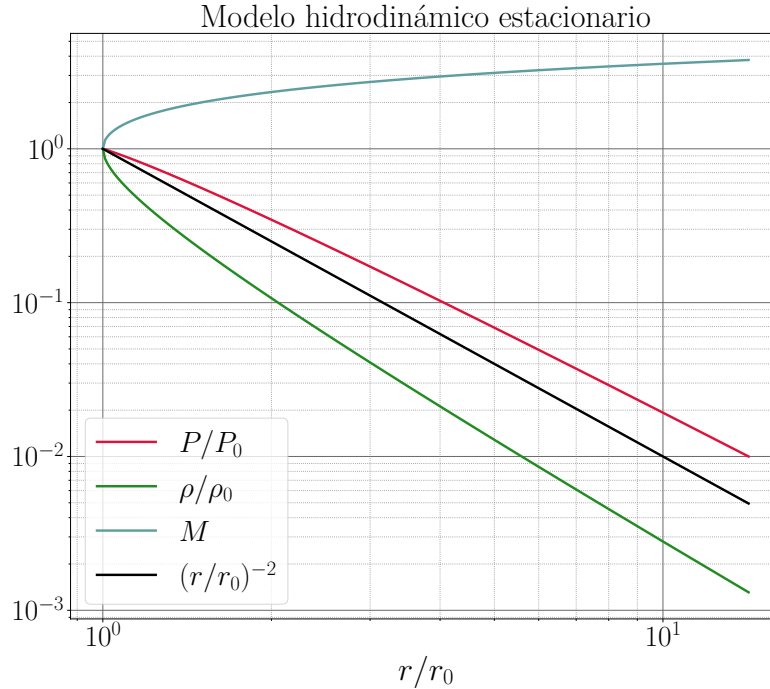


Figure 2.5: Normalized Mach number  $M$ , density  $\rho$ , and total pressure  $P$  as functions of  $r/r_0$ . A reference decline  $\sim r^{-2}$  is also shown (black line). Note that the density falls more steeply than  $r^{-2}$ , while the total pressure declines more slowly; in both cases this is due to the acceleration of the flow.

## 2.4 Conditions for the shocked shell

In their description of the interaction between two hypersonic flows, Cantó et al. (1996) derive solutions for different parameters  $\beta = (\dot{M}_w^0 v_w) / (\dot{M}_{w1}^0 v_{w1})$ , which is the ratio of the momentum fluxes of flows w and w1. This can be seen in Figure 2.6, where we note that when the momentum of one flow is much greater than that of the other, the shocked shell becomes highly curved and lies closer to the source with the weaker momentum flux.

Figure 2.7 shows the different types of pressures in each zone of this interaction between supersonic flows. At the discontinuity (the gray line in Figure 2.7), the pressure is the sum of the stellar wind RAM pressure,  $P_{\text{RAM}}$ , and the thermal pressure of the stellar wind. Since the stellar winds of Wolf-Rayet stars can reach velocities of order  $1 \times 10^3 \text{ km s}^{-1}$ , the Mach number of the stellar wind can be of order 100, so we will assume that  $P_{\text{DC}} = P_{\text{RAM}}$ . On the other hand, for the shocked shell (zone 2 of Figure 2.1), double pressure equilibrium must

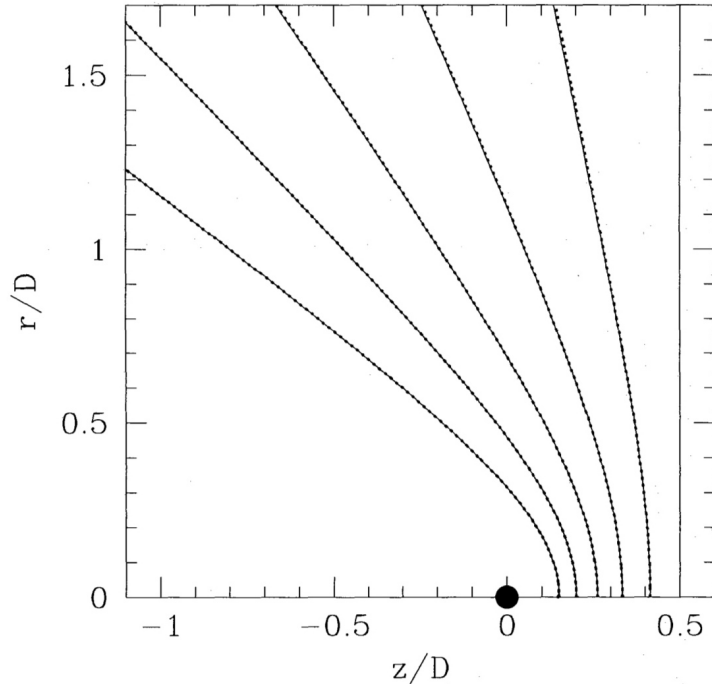


Figure 2.6: Shapes of shocked shells for different values of the parameter  $\beta$ . The vertical line at  $z/D = 0.5$  corresponds to  $\beta = 1$ , while the other curves correspond to 0.5, 0.25, 0.125, 0.0625, and 0.03125. The smaller the  $\beta$ , the more curved the shocked shell becomes. The other source is located at  $z/D = 1$  (Cantó et al., 1996).

hold. First, the pressure in the shocked shell,  $P_{\text{shell}}$ , must equal the pressure of the photoevaporative flow immediately upstream of the shock, i.e.,  $P_{\text{shell}} = P$ . Second, the pressure in the shocked shell must equal the RAM pressure of the shocked stellar wind.

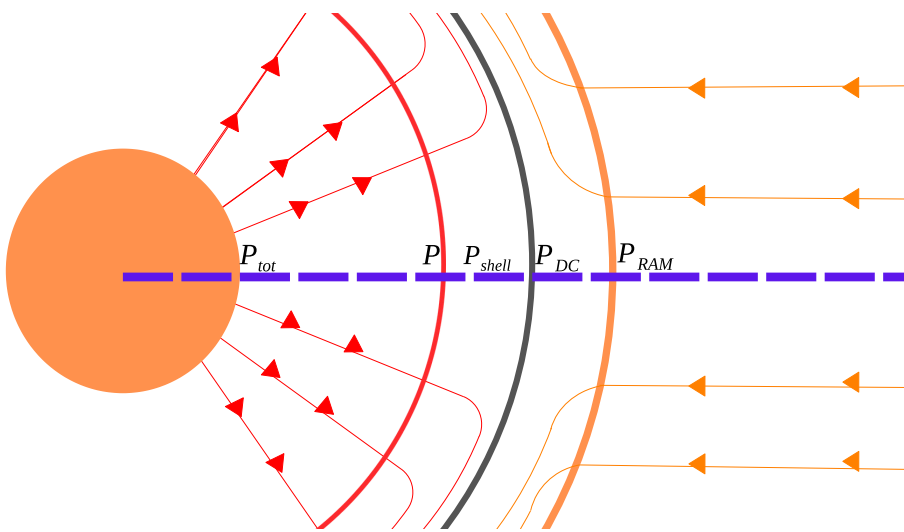


Figure 2.7: The base of the globule is dominated by the total pressure, equation (2.5). Along the red line, which is the innermost part of the shocked shell, the pressure is dominated by the thermal pressure of the photoevaporative flow,  $P$ . Along the orange line the pressure is dominated by the RAM pressure of the stellar wind,  $P_{RAM}$ , which is the only external pressure we are considering. At the discontinuity there is a pressure  $P_{DC}$ , which is the sum of the stellar wind RAM pressure and the thermal pressure of the shocked stellar wind.



## Chapter 3

# Globules in the M1-67 nebula

We now describe how we identified the globules in the M1-67 nebula. In Figure 3.1 (right panel) we see how these globules can be visually recognized by three key components: the globule itself appearing as a white circle; its pink tail, located immediately behind the globule in the direction opposite to the star; and its shocked shell, visible in gray. In this way we were able to identify a total of 168 globules.

From the observations we see that these globules have typical sizes of 200–300 milliarcseconds ( $5\text{--}7 \times 10^{-3}$  pc) in diameter, which are relatively small compared to the circumstellar nebula as a whole, whose size is  $\sim 60''$  (1.57 pc).

The globules can be located by their angular position and separation from the star. The angular position is the angle  $\phi$  measured with respect to the red line in Figure 3.2, which defines the zero-degree reference. The angle  $\phi$  is measured counterclockwise. The separation between the globule and the star is measured directly from the observations. Figure 3.2 shows an example of how we determine the angular position and separation for each globule.

In Figure 3.3 (left) we see the spatial distribution of the globules in the nebula: green points are the globules we identified, and the red line is the reference used for angular position. On the right we show their distribution as a function of separation and angular position. Certain symmetries can be discerned. For example, in the histogram at the top of the right-hand panel many globules are concentrated at two particular angular positions,  $\sim 90^\circ$  and  $\sim 200^\circ$ , whereas at  $120^\circ$  and  $300^\circ$  almost no globules are found. In the histogram on the right we see an apparently bimodal distribution in separation, with peaks at  $11''$  (0.28 pc) and  $17''$  (0.44 pc). This distribution indicates that the number of globules does not decline smoothly with distance, but instead that groups of globules are responsible for the peaks in the distribution.

Figure 3.4 shows a variety of globules in a small region, illustrating the different morphologies they present in different filters.

As noted earlier, the interaction between the globules' photoevaporative flows and the stellar wind produces a shocked shell, which we can see owing to recombinations, appearing as emission in some filters. For example, the

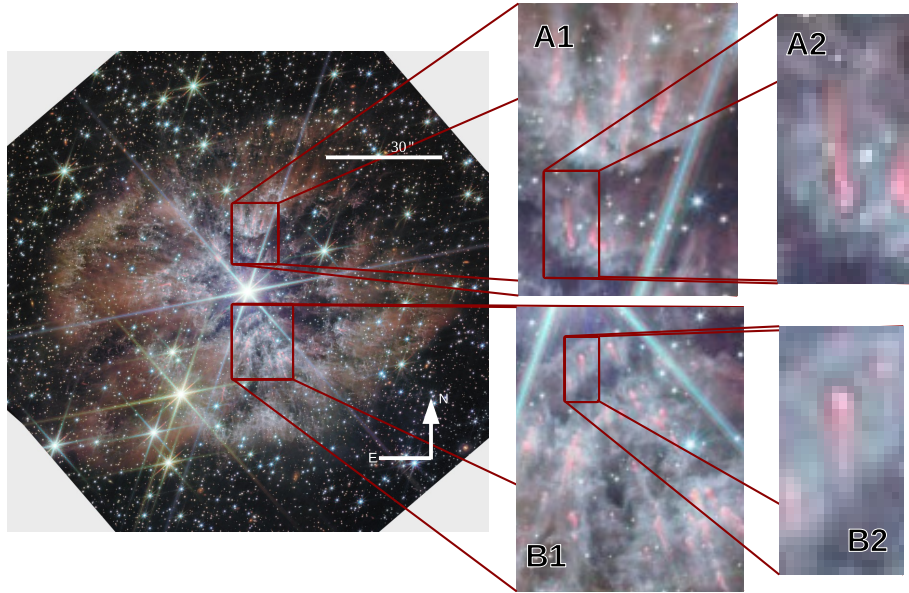


Figure 3.1: Image of the M1-67 nebula captured with JWST showing globules throughout most of the nebula. Zooming in on individual globules (white and pink emission) reveals their morphology in the neutral component, traced by PAH emission, while the gray color indicates their interaction with the star and its stellar wind. Insets A1, A2, B1, and B2 have dimensions of  $11.86'' \times 15.65''$  ( $0.31\text{ pc} \times 0.41\text{ pc}$ ),  $2.94'' \times 5.76''$  ( $0.07\text{ pc} \times 0.15\text{ pc}$ ),  $15.82'' \times 19.21''$  ( $0.41\text{ pc} \times 0.5\text{ pc}$ ), and  $2.42'' \times 4.53''$  ( $0.06\text{ pc} \times 0.11\text{ pc}$ ), respectively.

shocked shells around the globules are visible in the HST F656N filter and in the JWST F090W and F444W filters. We also constructed composite images to isolate the emission from ionized gas (see Appendix D). In the ionized-gas image, the shocked shell is more clearly visible.

In the JWST F1130W filter we can see what appear to be parts of the globule tails. Some appear smaller than others. In some cases, when globules are very close together, their tails seem to merge, and in some instances the tails appear to interact with other globules. In this filter we can also faintly see what may be the interaction between the ionized gas flow and the stellar wind.

We also created a composite to isolate the emission from neutral gas (see Appendix D). In this case the morphology of the globules is revealed more clearly, allowing us to better determine their properties.

With the wide variety of images available we can make many comparisons, viewing the globules in different filters and at different resolutions, which offers several advantages. For example, JWST observations provide higher spatial resolution, whereas the HST F656N filter, being very narrow, is less affected by stellar emission, unlike the JWST observations.

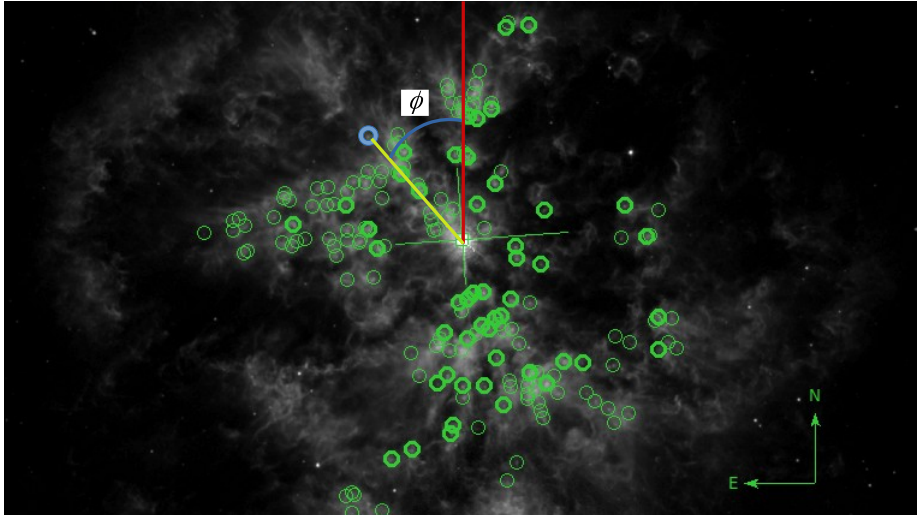


Figure 3.2: Example of how we obtained the angular position and separation with respect to the star. The blue circle marks the globule used as an example; the angle  $\phi$  with respect to the red line is the angular position, measured counterclockwise. The separation is the length of the yellow line connecting the globule (blue circle) with the star, located at the center of the image. The green points mark the positions of the other globules.

### 3.1 Estimating the RAM pressure of the stellar wind

In this work we consider only the RAM pressure of the stellar wind from WR 124 as the external confining pressure for the shocked shells surrounding the interacting globules. We write this as

$$P_{\text{RAM}} = \frac{\dot{M} v_\infty}{4\pi R^2}, \quad (3.1)$$

where  $\dot{M}$  is the stellar mass-loss rate,  $v_\infty$  the terminal wind velocity, and  $R$  the distance from the globule to the star. The first two parameters are given in Table 1.1, and for  $R$  we consider the separation range 0.1–0.9 pc, since the measured separations of the globules from the star fall within this interval. The distance is obtained as

$$\left[ \frac{R}{\text{AU}} \right] = \left[ \frac{D}{\text{pc}} \right] \left[ \frac{\theta}{\text{arcsec}} \right], \quad (3.2)$$

where  $\theta$  is the angular separation measured directly from the observations and  $D$  is the distance from us to the star. Figure 3.5 shows how the RAM pressure of the stellar wind varies as a function of distance.

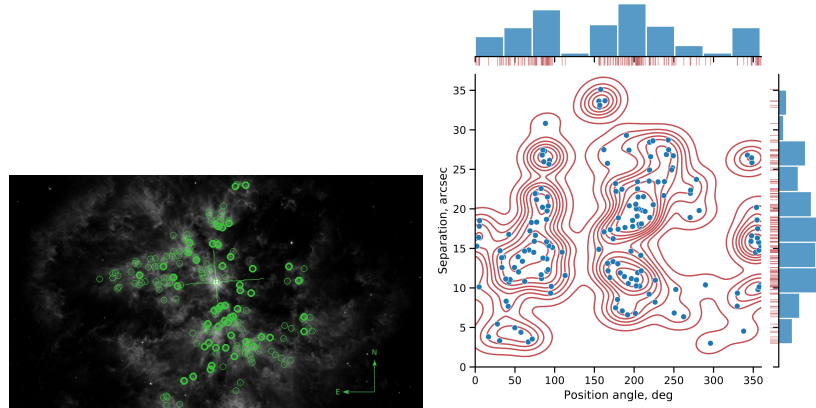


Figure 3.3: Left: positions of the globules in the M1-67 nebula (green points). The red line is the reference used to define the angular position of each globule. Right: distribution of the globules (blue points) as a function of separation and angular position. The upper panel shows the histogram of angular positions, while the right panel shows the histogram of separations. The red contours are smoothed density isocontours of the point distribution.

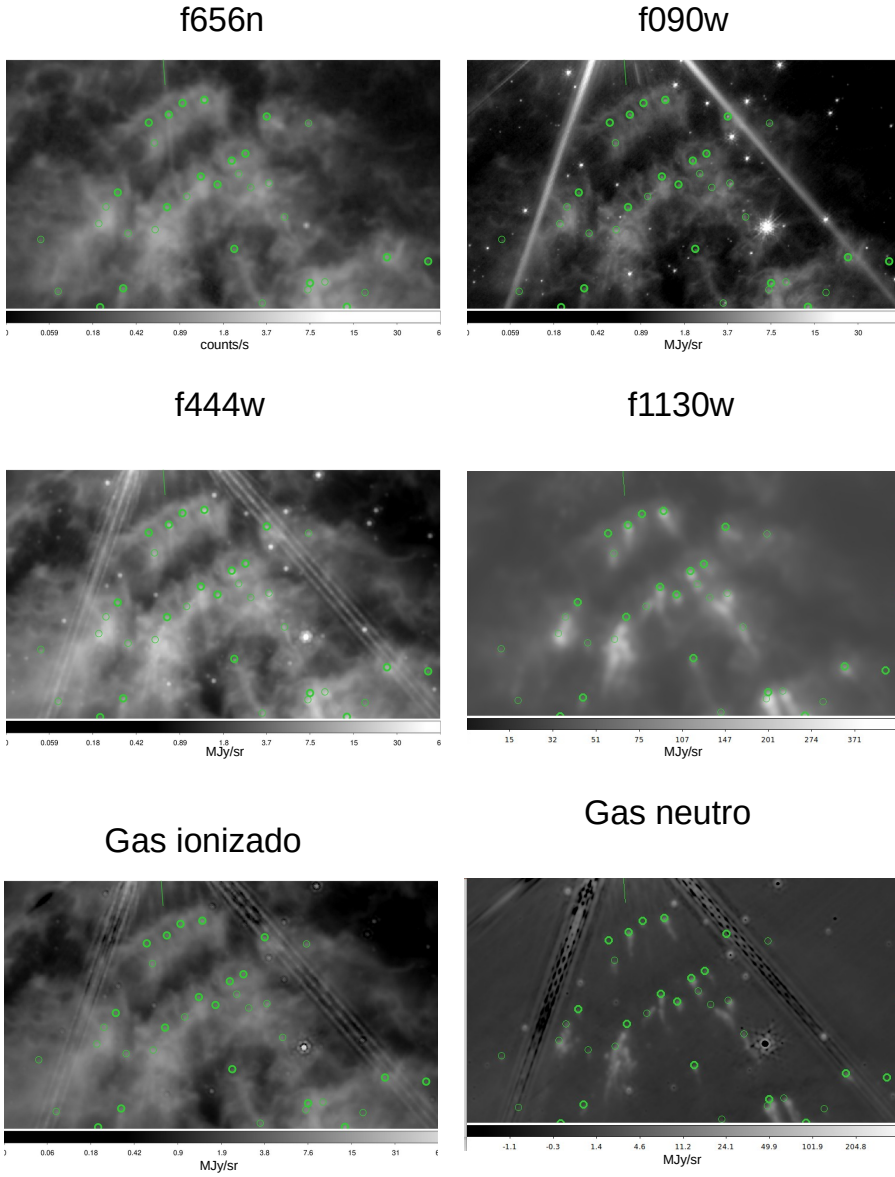


Figure 3.4: Top left: HST image of H $\alpha$  emission with the F656N filter. The other panels are JWST images with different filters. For ionized gas the following composite was used: f444w-0.43 f335m-0.16(f150w-0.6 f210m). For neutral gas the composite used was 1.4(f150w-0.6 f210m)+f335m-0.95 f210m. Green circles mark the globules.

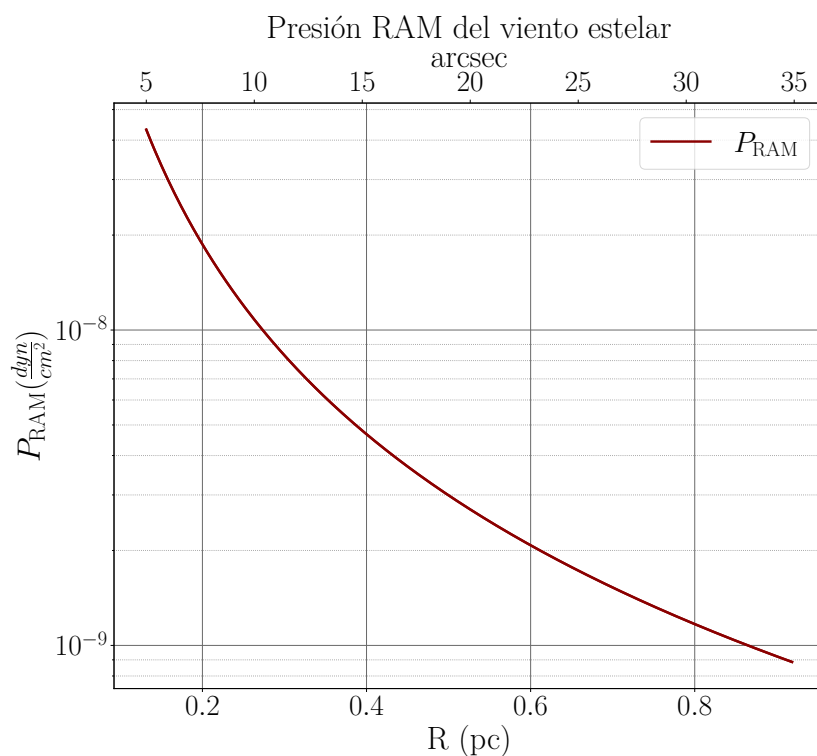


Figure 3.5: RAM pressure of the stellar wind from WR 124 as a function of distance in parsecs.

## Chapter 4

# Model fitting to brightness profiles

In this chapter we use the various observations to measure the sizes of the globules, their shocked shells, and the widths of those shells. We can also measure the brightness at the center of the globule and in the shocked shell, which will later allow us to estimate the density of the ionized gas in the shocked shell.

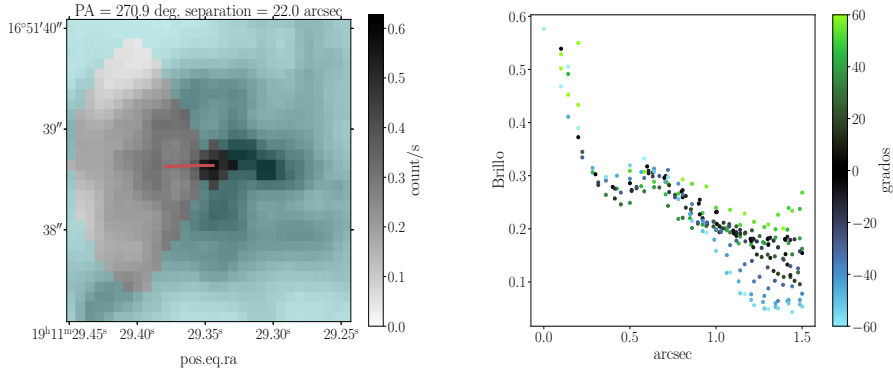
The measurements of the different parameters for the 168 identified globules are carried out as follows. Once the globule positions are known, we locate the peak of H $\alpha$  emission, which we define as the center of the globule<sup>1</sup>. We then define the symmetry axis of the model (Figure 2.1) as the line connecting the center of the globule with the star. Since our main interest is to describe the globule and its shocked shell, we apply a mask to isolate these two components. This mask ensures that our measurements are not affected by the complex structure of the nebula or by nearby globules. The mask is defined as follows: we take only those pixels lying within 0.2'' of the globule center, and those within a maximum distance of 1.5'' and a maximum angle of 60° with respect to the symmetry axis. With these values the globules and their shocked shells are always included in the mask, and the chosen parameters yield reliable results for the different measurements.

We then plot the brightness of each pixel within the mask as a function of distance from the globule center, as shown in Figure 4.1. To these points we fit two Gaussians and a constant.

The fit is motivated as follows. The width of the first Gaussian, centered at zero, gives the size of the globule, assuming that the emission peak coincides with the globule center. The second Gaussian indicates the location and width of the shocked shell. We expect an emission peak in the shocked shell due to recombinations, hence the second Gaussian. The distance between the peaks of

---

<sup>1</sup>In the ionized-gas observations we have only an estimate of the globule size; in Section 4.1 we obtain a more realistic measurement of the globule size using neutral gas.



(a) Example of a mask used for the globules. The mask is defined by the gray-scale pixels, here using HST observations. The globule center is at the image center. The red line connects the globule center to the star (off to the left), defining the symmetry axis. Pixels within a circle of 0.2'' around the globule center are included, as well as those within 1.5'' and within 60° of the symmetry axis.  
(b) Brightness within the mask as a function of distance from the globule center, measured along the symmetry axis.

Figure 4.1: Left: example of the mask used for fitting brightness profiles (gray-scale pixels), here using HST observations. The globule center is at the image center. The red line connects the globule center to the star (off to the left), defining the symmetry axis. Pixels within a circle of 0.2'' around the globule center are included, as well as those within 1.5'' and within 60° of the symmetry axis. Right: brightness of the pixels included in the mask as a function of distance from the globule center and angle with respect to the symmetry axis. Green points correspond to pixels in the lower part of the left panel, blue points to pixels in the upper part within the mask.

the two Gaussians gives the radius of the shocked shell. Finally, the constant represents the mean background brightness in the region. In the fit we assign lower weight to pixels farther from the globule center and to those with larger angle from the symmetry axis, according to

$$w = \frac{\cos^2(\theta)}{(0.3 + r)^2}, \quad (4.1)$$

where  $\theta$  is the angle relative to the symmetry axis and  $r$  is the distance from the globule center. The fit is performed with the `fitting.LevMarLSQFitter`<sup>2</sup> package of `astropy.modeling`. A clearer example of these fits is shown in Figure 4.2.

The fitting procedure was applied to the HST observations and, for the JWST, to the F090W filter and to the composite image isolating ionized gas. In this way we obtained several independent measurements at different resolutions, providing greater confidence that we are indeed detecting a shell and measuring the sizes of the different fitted parameters.

<sup>2</sup>Documentation: <https://docs.astropy.org/en/latest/api/astropy.modeling.fitting.LevMarLSQFitter.html>

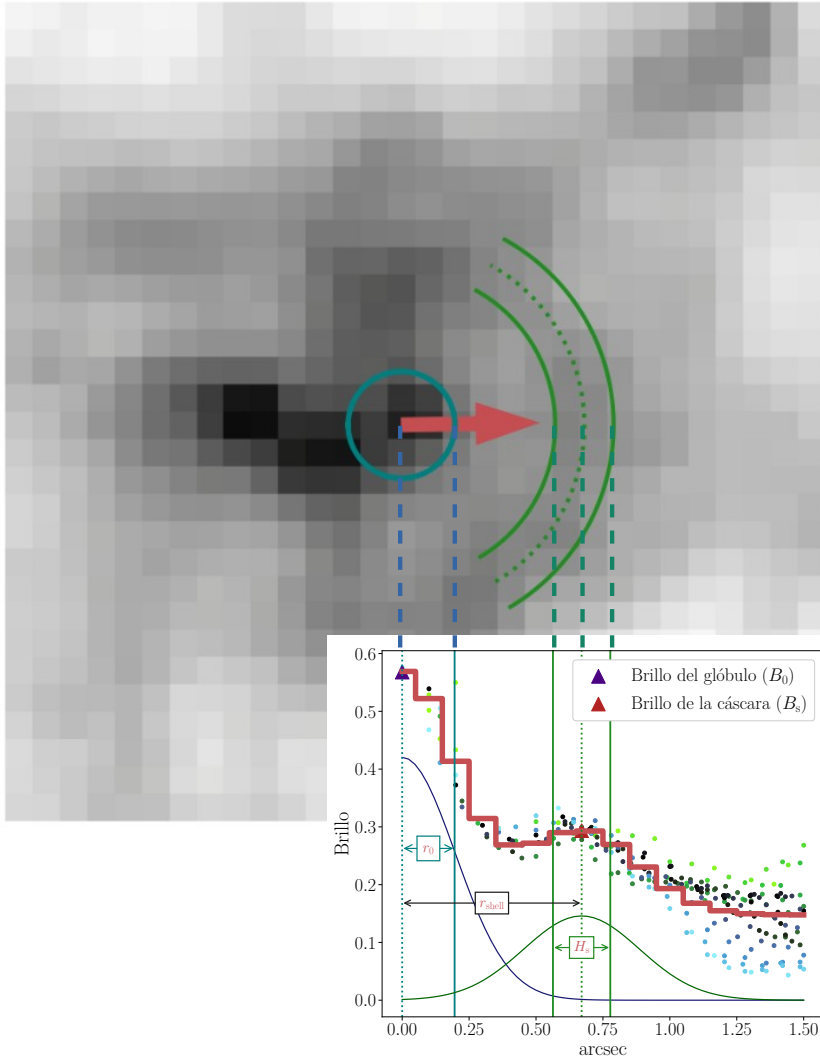


Figure 4.2: Example of the fit of two Gaussians plus a constant to the brightness profiles. This example is the same as in Figure 4.1, but for visualization the globule image has been rotated 180°. The internal and shell brightness values correspond to the peaks of the first and second Gaussians, respectively. The  $\sigma$  of the first Gaussian centered at zero gives the size of the inner region. The shell width is obtained from the  $\sigma$  of the second Gaussian. The shell radius is taken as the distance between the peaks of the two Gaussians. This fit is applied to the HST observations, and the figure shows how the fit appears directly on the image.

## 4.1 Measuring the radius in the neutral component

The previous fitting procedure was performed using images of ionized gas emission, so the measured radii did not accurately represent the neutral component. To measure the neutral gas we used a combination of the JWST filters F150W, F210M, and F335M to isolate neutral emission (see Appendix D). With this combination we avoid contamination of our measurements by field stars or by shocked shells.

In this case we fit only a Gaussian and a constant to the brightness profile, since the shocked shell is not visible here. The fitting was carried out as follows. Given that the mean radius of the globules from the previous fit was  $0.14''$  with a variation of  $\pm 0.04''$ , we placed a mask of  $0.2''$  around the emission peak together with cones of small opening angle. These cones are perpendicular to the symmetry axis of the model and extend  $1.5''$ . With this mask we expect the entire neutral emission to lie within the small circle, while the cones serve to better constrain the constant background level, since they are not affected by the wings of the globules. Figure 4.3 shows how the globule falls inside the mask without contamination from ionized gas emission or field stars.

With these fits we obtain the radius of the globules,  $r_0$ , the radius of the shocked shell,  $r_{\text{shell}}$ , and the width of the shocked shell,  $H_s$ . Since both  $r_0$  and  $H_s$  are measured using the  $\sigma$  of the fitted Gaussian (i.e. the RMS width of the profile), for comparison with instrumental widths our observed width is given by

$$W_{\text{obs}} = 2\sqrt{2 \ln 2} \sigma_{\text{obs}}, \quad (4.2)$$

where  $\sigma_{\text{obs}}$  is the measured value from the observations. Considering the point spread function (PSF) of each telescope, the intrinsic width is then

$$W_{\text{real}} = \frac{\sqrt{W_{\text{obs}}^2 - \Delta^2}}{2}, \quad (4.3)$$

where  $\Delta$  is the PSF of the telescope. For HST  $\Delta = 0.067''$ , and for JWST  $\Delta = 0.145''$  (for the filter combination used to observe only the ionized gas). In this way we obtain more realistic measurements of these two quantities.

## 4.2 Estimating uncertainties in the observational parameters

For the uncertainties we consider that they arise from inhomogeneities in the nebular brightness, unrelated to the globule or its shocked shell, or from systematic effects due to the limitations of the model, and not from photon noise. We therefore estimate these errors by comparing different measurements, assuming they are independent.

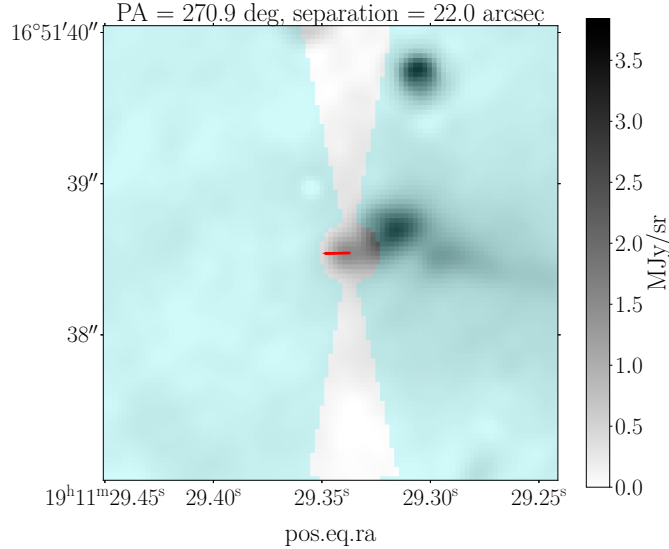


Figure 4.3: Example of the mask used to measure the radius of the neutral component of a globule. The mask is defined by the gray-scale pixels. To observe only neutral gas emission (PAHs), we used the combination of filters F150W, F210M, and F335M. The data are JWST observations.

#### 4.2.1 Uncertainties in $r_{\text{shell}}$ and $H_s$

For the radius and width of the shell,  $r_{\text{shell}}$  and  $H_s$ , respectively, we note that they follow a consistent trend (see Figure 4.4) when comparing the measurements obtained with HST and JWST. For these measurements we adopt the RMS uncertainty

$$\sigma = \frac{\sqrt{\text{Var}(x_J - x_H)}}{\sqrt{2}}, \quad (4.4)$$

where  $x_J$  are the measurements from JWST using the ionized gas composite, and  $x_H$  are the measurements from HST in  $\text{H}\alpha$  (see Appendix E).

#### 4.2.2 Uncertainty in $r_0$

For the inner region we have one measurement of the neutral radius using a JWST filter combination, and an approximate measurement with HST, since the latter traces only ionized gas while the globule is mainly neutral. Although there is not a strong correlation between the two measurements (see Figure 4.5), their mean values and standard deviations are very similar. We therefore adopt a single radius for all globules: 0.135'', the average of the two mean values. As

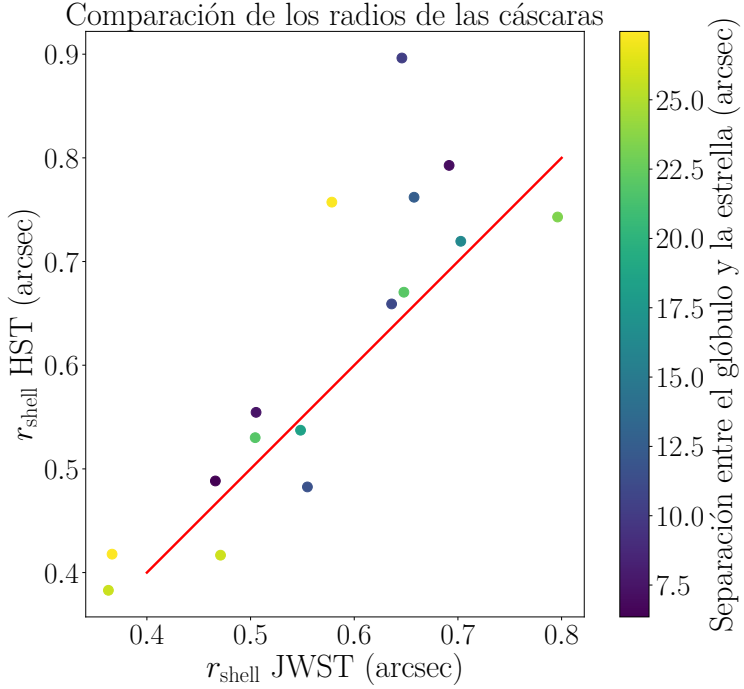


Figure 4.4: Comparison of shell radii (colored points) obtained from fits to both telescopes. Each point represents a globule for which a shell was detected in both instruments. The HST measurements are in the F656N filter, and the JWST measurements use the ionized-gas composite. The red line shows the 1:1 relation, indicating that the two sets of measurements are very similar.

the uncertainty we adopt the standard deviation of both measurements, which is the same,  $\pm 0.03''$  (see Figure 4.5).

#### 4.2.3 Uncertainties in $B_s$ and $B_0$

For the surface brightnesses of the shocked shell and the globule,  $B_s$  and  $B_0$ , respectively, we estimate the error as the following standard deviation:

$$\epsilon_B = \sqrt{\text{Var}((y - \bar{y})^2, w * w_2)}, \quad (4.5)$$

where  $y$  is the brightness profile from the HST F656N filter minus the fitted brightness profile,  $w$  is the weight from the model (equation 4.1), and  $w_2$  is the fitted Gaussian corresponding to the component in question. For the inner part

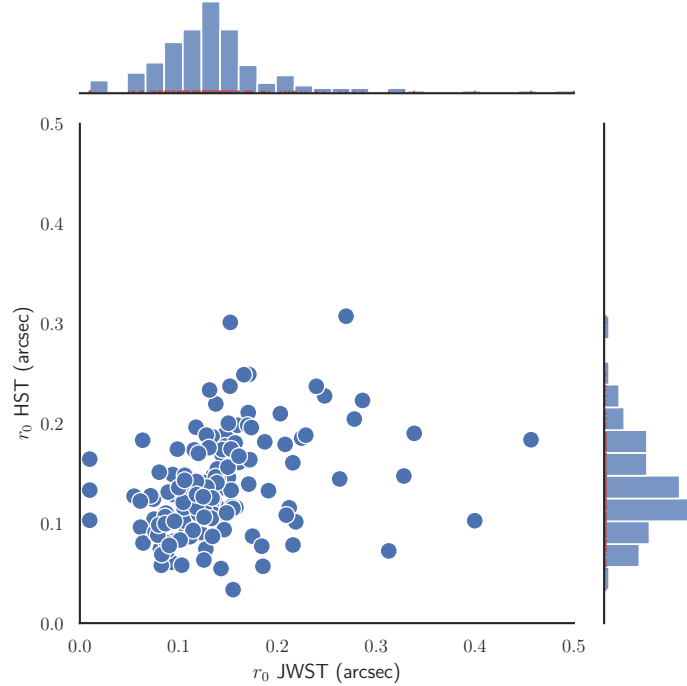


Figure 4.5: Comparison of the radii of the neutral component measured with both instruments. The upper histogram shows the JWST measurements, with a mean value of  $0.15''$  and a standard deviation of  $0.03''$ . The right-hand histogram shows the HST measurements, with a mean of  $0.12''$  and a standard deviation of  $0.03''$ .

$w_2$  is the first Gaussian centered at  $0''$ ; for the shell  $w_2$  is the second Gaussian (see Figure 4.2).

With these uncertainty estimates we use the `uncertainties`<sup>3</sup> package to compute the error bars. This package calculates uncertainties using the theory of linear error propagation, taking into account whether the data are fully independent or correlated.

---

<sup>3</sup>Documentation: <https://pythonhosted.org/uncertainties/>

### 4.3 Estimating the ionized gas density from H $\alpha$ surface brightness

To estimate the density of the ionized gas, we first use the definition of the emission measure (EM):

$$\text{EM} = \int_z n_i n_e dz, \quad (4.6)$$

where  $n_i$  is the ion density,  $n_e$  the electron density, and the integral is along the line of sight ( $dz$ ). If we consider a fully ionized gas in which the electrons come only from hydrogen, then  $n_e = n_i = n^4$ . Thus  $\text{EM} = n^2 l$ , where  $n$  is the RMS mean density and  $l$  is the depth of the dense gas along the line of sight.

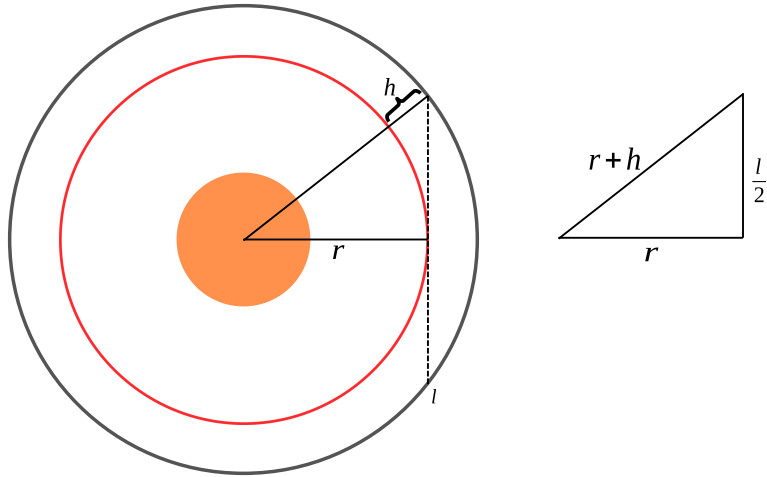


Figure 4.6: Schematic diagram showing a line of sight, with maximum path length  $l$  (dashed line). Assuming spherical symmetry we obtain this configuration, where  $h$  is the width of the shocked shell,  $r$  is the radius from the globule center to the onset of the shocked photoevaporative flow, and  $h < r$ .

Assuming a spherical shell of radius  $r$ , thickness  $h$  with  $h \ll r$ , and constant density, we obtain

$$\text{EM} = 2\sqrt{2rh} n^2. \quad (4.7)$$

From Figure 4.6 we see that by geometry  $r^2 + \left(\frac{l}{2}\right)^2 = (r+h)^2 = r^2 + 2rh + h^2 \approx r^2 + 2rh$ , hence  $l = 2\sqrt{2rh}$ . Therefore, using the EM we have

$$n = \sqrt{\frac{\text{EM}}{l}} = \sqrt{\frac{\text{EM}}{2\sqrt{2rh}}}. \quad (4.8)$$

---

<sup>4</sup>There is in principle also a contribution from He, but we treat it as neutral because the star emits too few energetic photons to ionize He, compared to the ionizing photon rate for H (Jiménez-Hernández et al., 2020).

In this work we apply this method to the detected shells, taking  $r = r_s$  and  $h = H_s$ .

### 4.3.1 Using EM from the observations

In our HST observations the surface brightness is given in units of counts s<sup>-1</sup>. We use a conversion factor of 0.0137 to obtain units of erg s<sup>-1</sup> cm<sup>-2</sup> sr<sup>-1</sup> (see Appendix F). Dividing by the energy of an H $\alpha$  photon we have

$$B \frac{0.0137}{(h\nu)_{H\alpha}} = \int \frac{f_{H\alpha} \alpha_B n_e n_p}{4\pi} dz, \quad (4.9)$$

where  $B$  is the observed surface brightness,  $(h\nu)_{H\alpha}$  is the photon energy of H $\alpha$ ,  $f_{H\alpha}$  is the fraction of all recombinations to levels  $n \geq 2$  that result in H $\alpha$  emission,  $\alpha_B$  is the case B recombination coefficient,  $n_e$  is the electron density, and  $n_p$  the ion density. The integral on the right is along the line of sight.

If we take both  $f_{H\alpha}$  and the recombination coefficient as constants, then

$$B \frac{0.0137}{(h\nu)_{H\alpha}} = \frac{f_{H\alpha} \alpha_B}{4\pi} \int n_e n_p dz, \quad (4.10)$$

where the integral is the EM. Assuming  $f_{H\alpha} = 0.5$  and  $\alpha_B = 2.3 \times 10^{-13}$  cm<sup>3</sup> s<sup>-1</sup>, we obtain  $f_{H\alpha} \alpha_B = 1.17 \times 10^{-13}$  cm<sup>3</sup> s<sup>-1</sup>. The EM can then be derived directly from the observations as

$$\text{EM} = B \frac{0.0137}{(h\nu)_{H\alpha}} \frac{4\pi}{1.17 \times 10^{-13} \text{ cm}^3 \text{ s}^{-1}}, \quad (4.11)$$

which yields EM in units of cm<sup>-5</sup> (cgs).

It is important to note that in deriving the density from EM and  $l$ , we are assuming that  $l$  is perpendicular to the symmetry axis of the model.

In Figure 4.7 we show that the maximum density  $n_1$  lies along the symmetry axis and decreases with angle as  $\cos^{1/2} i$  (Tarango-Yong & Henney, 2018).

## 4.4 Good fits

For 16 globules we obtained good fits, since the measurements matched both the globules and the shocked shells that could be visually identified in the images. From these fits we now know  $r_0$ ,  $r_{\text{shell}}$ , and  $H_s$ . In addition, we have measured the brightness both in the inner region and in the shocked shell, so we can extract further information. In Section 4.3 we showed how to estimate the density in the shocked shell from its brightness, which then allows us to determine the shell pressure,

$$P_{\text{shell}} = \rho c_s^2. \quad (4.12)$$

This pressure can be compared with the RAM pressure of the stellar wind. We can also estimate the internal pressure of the globule and compare it directly with the model.

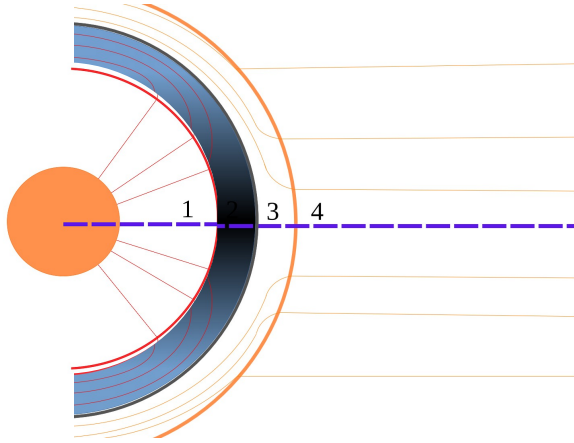


Figure 4.7: Along the symmetry axis the shocked shell has a maximum density  $n_1$  (darker color), which decreases with increasing angle from the axis (lighter color).

These well-fit globules span a wide range of separations from the star, so they provide a representative view of the nebula and the globules in general. Figure 4.8 shows examples of good fits, where the globule and its shocked shell are clearly identifiable.

## 4.5 Recovered fits

By fitting the brightness profiles from two telescopes with different resolutions, we obtained improved results. In some globules, even though their shocked shells were visible by eye, our algorithm failed to detect them in one of the two images.

Figure 4.9 shows examples where a possible shell can be seen visually, but the brightness-profile fit fails to detect it in one telescope (top left and bottom right panels), due to scatter in the data points or to too few points, as in the HST data. Another reason for poor detection was that the shell often had very low brightness.

In this way we increased the sample size beyond the initial set, resulting in a final sample of 30 globules for which we know the globule size, the shocked shell radius and width, and the surface brightness at the globule center and in the shocked shell<sup>5</sup>. With these measurements we can compare the pressure of the shocked shells with the RAM pressure of the stellar wind. Thus in Chapter 5 we will compare our model directly with the observations.

---

<sup>5</sup>All of these fits are shown in Appendix J

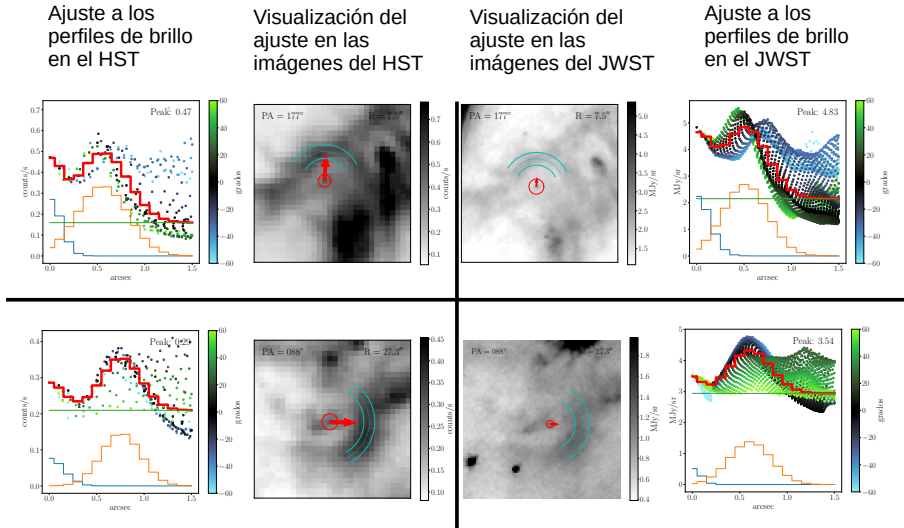


Figure 4.8: Examples of good fits. Left panels: brightness-profile fits (left subpanel) and the corresponding HST image (right subpanel). Right panels: JWST data. The fits shown are for the ionized-gas composite (Figure 3.4), but the visualizations are in the F090W filter, since its morphology is very similar to the HST images.

## 4.6 Discarded globules

Despite having a substantial number of globules suitable for applying the model, not all could be used. Some had poor fits due to the large scale structure of the nebula, contamination by background stars, or the diffraction spikes of bright stars. In such cases the neutral region or the shocked shell could not be reliably detected, or their sizes were incorrectly determined. Figure 4.10 shows examples of globules whose shocked shells could not be reliably measured.

Table 4.1 lists the mean values of the different measured quantities, taking the scatter among the globules as the uncertainty. The mean separation between the globules and the star is  $14.96 \pm 7.1''$ . The globule radius and shell width are both smaller than the shell radius. The density is typically of order  $10^3 \text{ cm}^{-3}$ , while the shell pressures are of order  $10^{-9} \text{ dyn cm}^{-2}$ . Finally,  $n_{i,0}$  is the ionized-gas density at the ionization front of the globules, assuming ionization equilibrium.

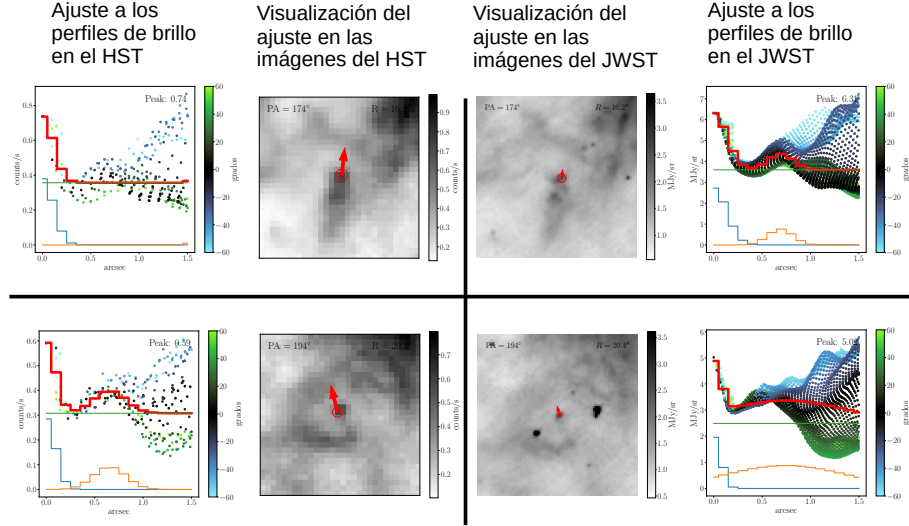


Figure 4.9: Examples of recovered fits. In these images the shell is visible by eye, but the brightness-profile fitting fails to detect the shocked shell in one telescope (top left and bottom right panels), due to scatter in the points.

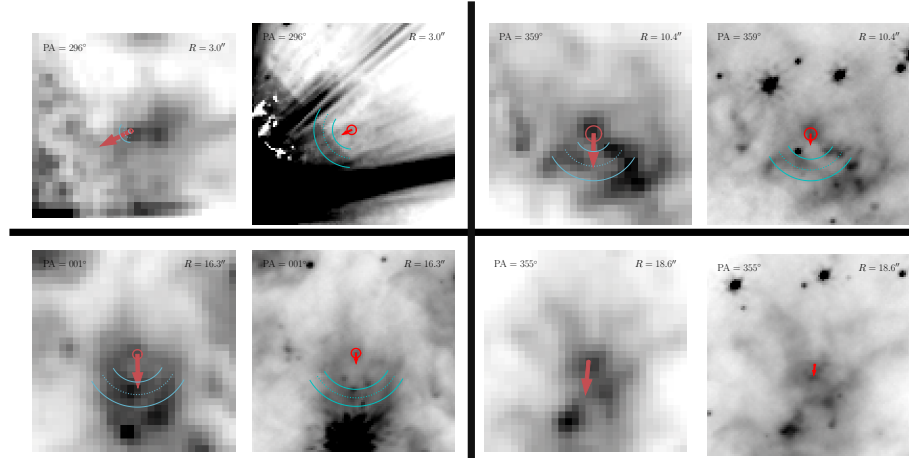


Figure 4.10: Examples of discarded globules. Left: HST images; right: JWST F090W filter. The first globule is discarded because it is affected by telescope diffraction and by the large-scale nebular structure, likely due to its proximity to the central star. In the other examples, nearby sources compromise the measurements of possible shocked shells.

Results of the good fits	
Separation	$14.96 \pm 7.1''$
Globule radius $r_0$	$0.135 \pm 0.03''$
Shell radius $r_{\text{shell}}$	$0.62 \pm 0.13''$
Shell width $H_s$	$0.24 \pm 0.1''$
$n_{\text{shell}}$	$1.37 \pm 0.05 \times 10^3 \text{ cm}^{-3}$
$n_{i,0}$	$5.01 \pm 0.55 \times 10^3 \text{ cm}^{-3}$
$P_{\text{shell}}$	$1.89 \pm 0.06 \times 10^{-9} \text{ dyn cm}^{-2}$
$r_{\text{shell}}/r_0$	$4.4 \pm 1$

Table 4.1: Mean values of the results obtained from the fits. The uncertainties are the scatter among different globules.



## Chapter 5

# Pressure balance in the shells

In this chapter we use the measurements obtained from the various observations of the globules in the M1-67 nebula. In this way we can investigate the pressure balance between the photoevaporative flow from the globules and the stellar-wind pressure, and finally compare directly with the stationary hydrodynamic model that we propose. If the observations are consistent with our model, then we will gain a better understanding of the spatial distribution of the globules in the M1-67 nebula.

We identified 168 globules in the nebula, distributed at distances of  $3\text{--}35''$  ( $7\text{--}92 \times 10^{-2}$  pc) from the central star. These globules appear either in groups or in isolation, as shown in Figure 3.3.

Although we could not obtain good fits for all the globules, we still have a very useful sample, as they are distributed over a wide range of distances from the star and show a wide variety in the measured parameters.

### 5.1 Internal pressure balance

We now compare directly with the model (see Figure 2.5). Specifically, we compare the ratio of the pressure in the shocked shell of the globule to that at the globule surface against the ratio of the shell radius to the globule radius. Recall that Figure 2.5 shows  $P/P_0$  as a function of  $r/r_0$ .

Since we are considering a stationary model, the pressure in the shocked shell—where we consider only the thermal pressure—must equal the total pressure just before  $r_{\text{shell}}$ . In Chapter 2 we showed that the model predicts  $f$  as a function of  $r/r_0$ , giving the pressure of the photoevaporative flow just before the shock, normalized by the pressure at the globule base, as a function of radius.

The ratio of the radii is straightforward, since we measured these parameters directly for each globule. Because we have also measured the brightness and sizes of both the globule and the shocked shell, we can calculate their respective densities.

For the ratio of the pressures at the globule base and in the shocked shell,

recall from Section 4.3.1 that  $B \propto EM = n^2 l$ , hence

$$\frac{B_s}{B_0} = \frac{n_s^2 l_s}{n_0^2 l_0}, \quad (5.1)$$

where  $B_s$ ,  $n_s$ , and  $l_s$  are the brightness, density, and line-of-sight depth (perpendicular to the symmetry axis) for the shell (see Figure 4.6), and  $B_0$ ,  $n_0$ , and  $l_0$  are the corresponding quantities for the inner region. For the observations we have  $f_{\text{obs}} = \frac{P_{\text{shell}}}{P_0} = \frac{\rho_{\text{shell}}}{2\rho_0} \Rightarrow \frac{\rho_{\text{shell}}}{\rho_0} = 2f_{\text{obs}}$ , so

$$\frac{B_s}{B_0} = 4f_{\text{obs}}^2 \frac{l_s}{l_0} \Rightarrow f_{\text{obs}} = \frac{1}{2} \left( \frac{B_s/B_0}{l_s/l_0} \right)^{1/2}. \quad (5.2)$$

In this way we can compare directly with the model. Appendix G gives details of the brightness corrections.

Because the globules are very small, we take  $r_0 \approx l_0$ <sup>1</sup>. Thus the comparison with the model follows directly from the observations.

Figure 5.1 shows that the observational results closely match the predictions of the proposed model. The observations fall mostly in the range  $r_{\text{shell}}/r_0 = 3\text{--}6$  (the ratio of shell radius to globule radius), while the pressure ratios fall in the range  $f_{\text{obs}} = 0.05\text{--}0.15$ . The observed data also show a scattered anti-correlation.

Since the model has no free parameters and the observational results agree well with its predictions, we conclude that the model provides a valid explanation of the interaction between the supersonic flows. In Figure 5.1 we see that the observational measurements of  $f_{\text{obs}}$  are consistent with the model predictions  $f_{\text{model}} = P/P_0$  (equation 2.6), within the error bars.

## 5.2 External pressure balance

In Figure 5.2 we plot the shell pressure of the globules as a function of their projected separation from the star. The purple points show the shell pressures, while the red line shows the RAM pressure of the stellar wind. We see that the globule shell pressures fall below the stellar-wind RAM pressure if the projected separation is taken as the true separation. In our model, however, the shell pressure must be in equilibrium with the RAM pressure, so the observed separation is likely only a projected one.

If the globule is projected by an angle  $i$  (see Figure 5.3), then

$$R \cos i = R_p, \quad (5.3)$$

where  $R$  is the true separation from the star,  $i$  the inclination angle, and  $R_p$  the projected distance that we observe. Note that the shell pressure equals the stellar-wind RAM pressure only along the symmetry axis, and as seen in

---

<sup>1</sup>From Section 4.3.1 we have  $l_0 = 2\sqrt{2hr} = 2\sqrt{2h/r_0}r_0 = 0.98r_0 \approx r_0$ , using  $h/r_0 \approx 0.12$  (see Appendix C).

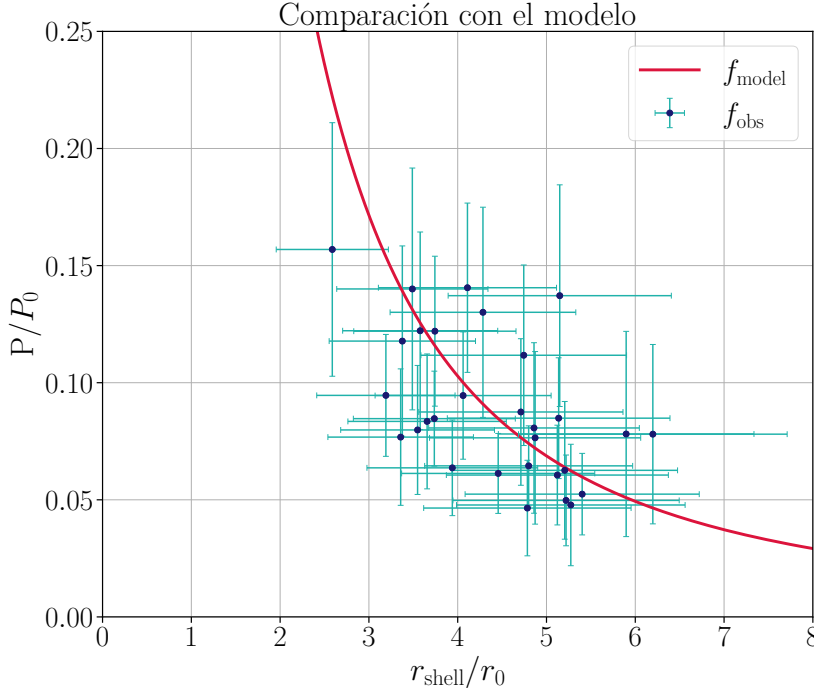


Figure 5.1:  $f_{\text{model}}$  is the theoretical curve obtained from the proposed model, while  $f_{\text{obs}}$  is the ratio between the pressure in the shocked shell and the pressure at the globule surface from the observations.

Section 4.3.1, off the axis the shell pressure decreases by a factor of  $\cos^{1/2} i$  (Tarango-Yong & Henney, 2018). Thus, including this inclination factor, we have

$$P_{\text{shell}}(i) = \rho \cos^{1/2}(i) c_s^2 \Rightarrow P_{\text{shell}}(i) \cos^{-1/2}(i) = \rho c_s^2, \quad (5.4)$$

and therefore

$$P_{\text{shell}}(i) \cos^{-1/2}(i) = \frac{\dot{M}v_\infty}{4\pi R_p^2} \Rightarrow P_{\text{shell}}(i) = \frac{\dot{M}v_\infty}{4\pi R_p^2} \cos^{5/2} i. \quad (5.5)$$

With this equation we can determine  $\cos i$ , since we know both the shell pressure and its projected separation. Substituting into equation 5.2 then yields the true separation of the globule from the star, and thus the real distribution of globules by distance.

In Figure 5.4 we see that the globule shell pressures can be matched to the RAM pressure by adopting an inclination angle  $i$ . From this we can determine the inclination angle for each globule.

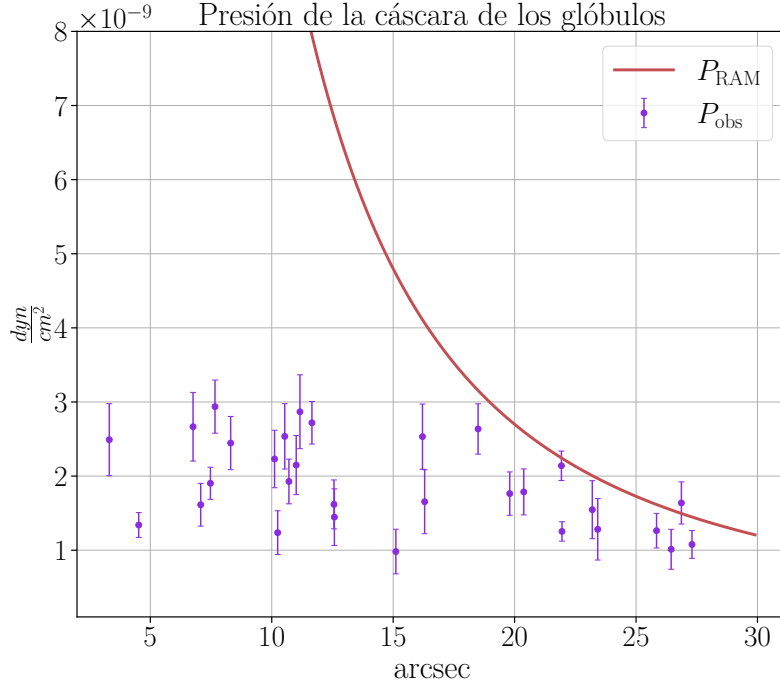


Figure 5.2: Shell pressures of the globules (purple circles) compared with the stellar-wind RAM pressure (red line), assuming the projected separation equals the true separation.

In Figure 5.5 the solid lines show the case where the shell density does not decrease with angle, i.e.  $P_{\text{shell}}(i) = \frac{\dot{M}v_\infty}{4\pi R_p^2} \cos^2 i$ . At small inclination angles the solid lines nearly coincide with the dashed lines (where the density decreases with angle), so the difference is small. At larger angles, however, the difference becomes significant. We also note that at large distances the solid and dashed lines converge, which may indicate that for globules farther from the star the true and projected separations are nearly equal. We discuss this further in the next chapter.

Table 5.1 lists the mean values obtained when accounting for the inclination angle, assuming that the density decreases with angle. Since the mean value of  $\cos(i)$  is 0.65, we can conclude that we are indeed seeing projected separations for nearly all the globules. In reality they are farther from the star than they appear in the images. Figure 5.6 shows histograms of the projected (orange bars) and true (blue bars) separations of the globules. While many globules appeared close to the star, the true separations are all greater than  $10''$  (0.26 pc). There

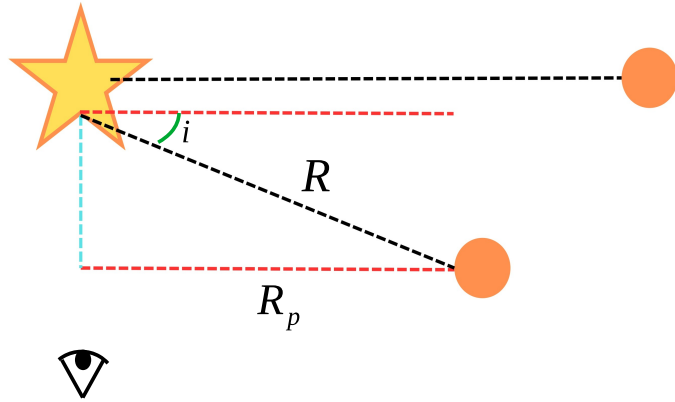


Figure 5.3: Illustration of how some globules are affected by an inclination angle relative to our line of sight. For the lower globule the true distance to the star is  $R$ , while we observe  $R_p$ , the projected distance at angle  $i$ . The upper globule is not affected by projection.

is also a concentration of globules at  $\sim 17''$  (0.44 pc).

Results with inclination angle	
$\cos(i)$	$0.65 \pm 0.01$
$R$	$22.08 \pm 0.34''$
$n_{\text{shell}}(i)$	$1.81 \pm 0.05 \text{ cm}^{-3}$
$P_{\text{shell}}(i)$	$1.89 \pm 0.06 \times 10^{-9} \text{ dyn cm}^{-2}$

Table 5.1: Typical values of the results obtained when accounting for the inclination angle  $i$ .

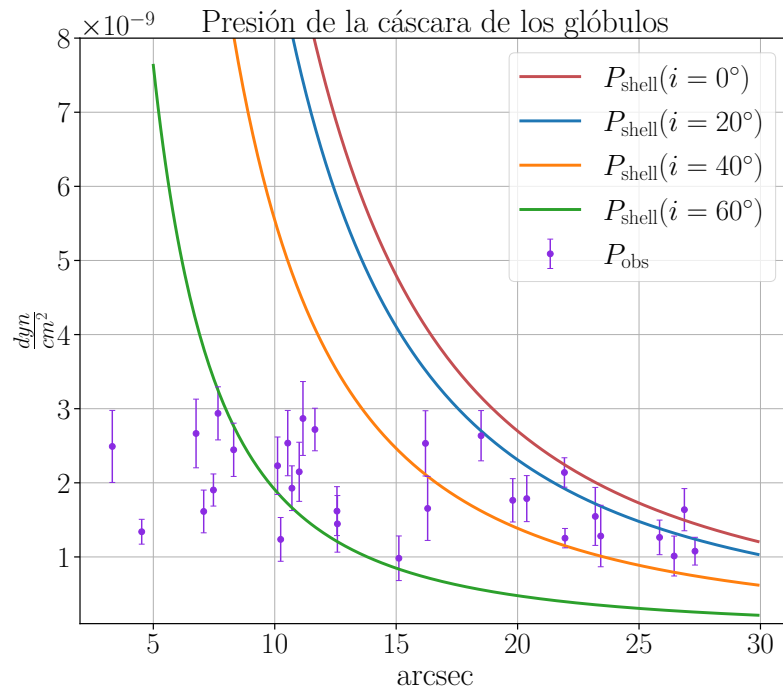


Figure 5.4: Examples showing how the inclination angle of each globule can be determined by adjusting the shell pressure (purple circles) so that it matches the stellar-wind RAM pressure (solid lines).

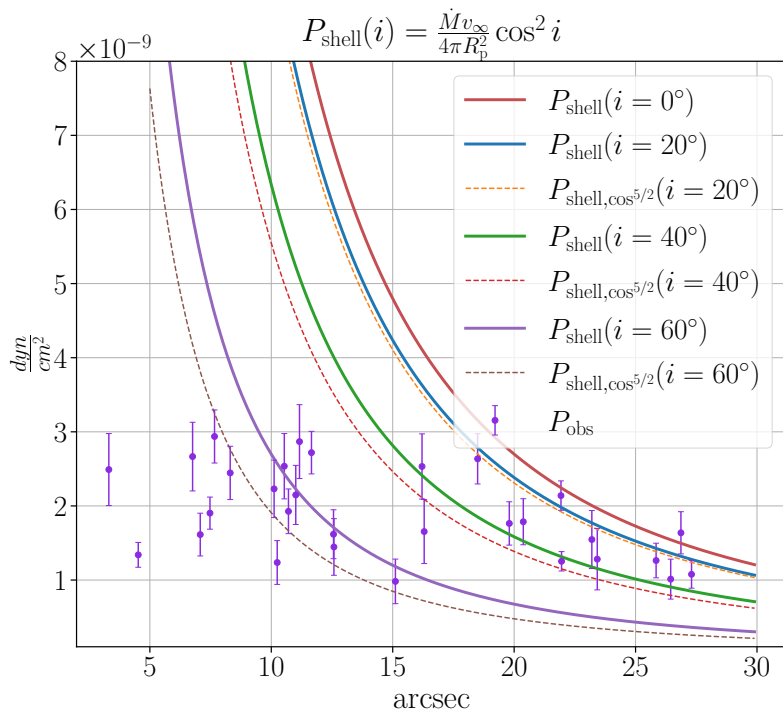


Figure 5.5: The solid red line shows the stellar-wind RAM pressure as a function of true distance. The other solid lines show shell pressures for different inclination angles  $i$ , assuming the shell density does not decrease with angle. The dashed lines show shell pressures assuming the density decreases with angle as  $\cos^{-1/2}(i)$ .

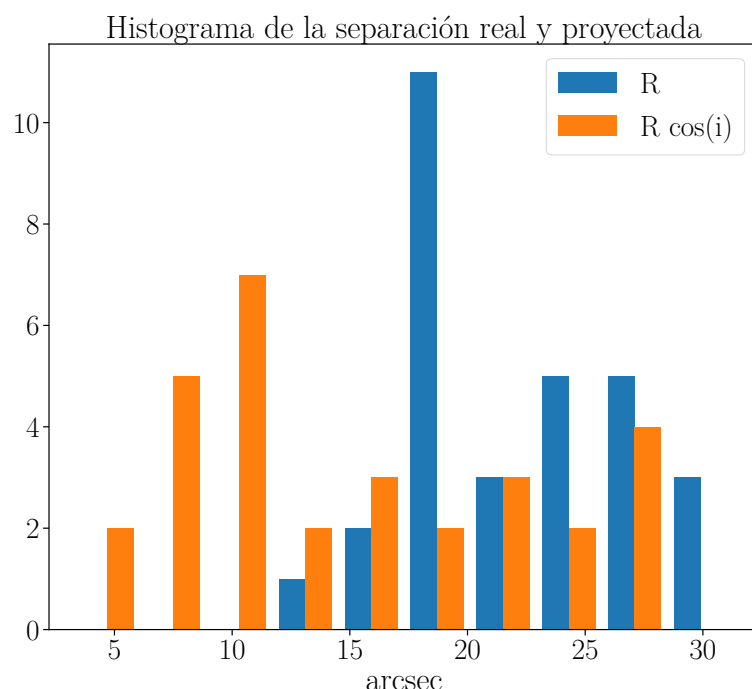


Figure 5.6: Histograms of the true separations (blue) and projected separations (orange) of the globules, measured in arcseconds.

# Chapter 6

## Discussion

Here we discuss several issues that arose when fitting the brightness profiles, as well as some properties of the globules, among other points. Since there are multiple topics to cover, we divide the discussion into sections.

Given that Zavala et al. (2022) estimate that the circumstellar nebula was formed about  $11.8 \times 10^3$  yr ago, we may suppose that the phases described in Section 1.1 have already occurred. This is important because, if the system were in a different phase—such as the implosion phase—then the radii would be changing and the pressures we consider might not yet be in equilibrium. If the pressure balance had not yet been reached, that would indicate that the interaction between the photoevaporative flow and the stellar wind formed only recently.

### 6.1 Identification of globules and their shells

Although the presence of globules and their interaction with the stellar wind is apparent in the JWST images, the situation is not always clear, since some globules are found in groups, as in Figure 6.1. In such cases, detecting the shocked shell is more challenging for several reasons. In the upper panel of Figure 6.1 we see a clear example of how two very nearby globules can be mistaken for a single object, as for those marked with blue circles. This can lead us to misidentify the size of the neutral part of the globule and overestimate it. Behind these globules lie two more nearby globules (black circles); due to projection on the sky they appear in the wakes of the blue-circled globules, so at first glance we might be unable to detect a distinct shocked shell. The globule marked with a red circle is smaller than the others in the group; its shocked shell appears very close to it, but in reality this shell seems to belong to the pair marked with blue circles. Something similar happens for the globule marked with a green circle, which apparently lacks a shell but seems to lie within the shocked shell of another globule.

In the lower panel of Figure 6.1 we again see a group of globules, but this

time they are sufficiently separated that their respective shells are not confused. The problem here is that the shells are close enough to one another that the emission from one affects the others. In this particular example, the larger shells contaminate the smaller ones in terms of their emission.



Figure 6.1: Examples of globule groups found in the nebula. Top: several issues arise, including determining whether very close features are one or multiple globules, and identifying which shocked shell belongs to which globule when a shell is detected. Bottom: the proximity of globules causes the emission from one shocked shell to affect that of a nearby shell.

## 6.2 Mass of the globules

For the ionized-gas density, Grosdidier et al. (1998) analyzed the M1-67 nebula and found bright knots with sizes of  $0.2\text{--}0.3''$ , for which they estimated ionized-gas densities of  $4800\text{--}12\,000\,\text{cm}^{-3}$ . These bright knots appear to correspond largely to our identified globules. Their estimates are consistent with ours, for which we find a typical density of  $5 \times 10^3\,\text{cm}^{-3}$  (Table 4.1).

To estimate the density in the neutral part, we assume pressure equilibrium between the neutral and ionized components, so that

$$2n_{i,0}c_{s,i}^2 = n_n \left( c_{s,n}^2 + \frac{1}{2}v_A^2 \right), \quad (6.1)$$

where  $n_{i,0}$  and  $c_{s,i}$  are the density and sound speed, respectively, in the ionized part;  $n_n$  and  $c_{s,n}$  are the density and sound speed in the neutral part; and  $v_A$  is the Alfvén speed, defined as  $v_A = B/\sqrt{4\pi\rho}$  with magnetic field  $B$  and density  $\rho$ . Assuming the neutral part is magnetically dominated, we adopt  $v_A$  in the range  $1\text{--}3\text{ km s}^{-1}$ , corresponding to microgauss magnetic fields (Bertoldi, 1989). The neutral sound speed is  $0.5\text{ km s}^{-1}$  for a mean mass of  $1.3m_p$  and  $T = 300\text{ K}$ . Thus the density ratio

$$\frac{n_n}{n_{i,0}} = \frac{2c_{s,i}^2}{c_{s,n}^2 + \frac{1}{2}v_A^2} \quad (6.2)$$

lies in the range 42–266. To estimate the globule mass we therefore adopt  $n_n = 100n_{i,0}$ , which falls within this range, bearing in mind an uncertainty of roughly a factor of two. Assuming, as in the model, that the globules are spherical, the mass of each globule is

$$M_g = \frac{4}{3}\pi r_0^3 100 n_{i,0} m_H. \quad (6.3)$$

With these neutral densities we find an average mass of  $4.5 \times 10^{-3}\text{ M}_\odot$ . If we take this mean mass for all globules, the total mass of the 168 globules is  $168 \times 4.5 \times 10^{-3}\text{ M}_\odot = 0.75\text{ M}_\odot$ <sup>1</sup>, which is lower than the ionized-gas mass of  $1.33\text{ M}_\odot$  calculated by Grosdidier et al. (1998).

### 6.3 Three-dimensional distribution of the globules

Using long-slit spectroscopy in selected regions of the nebula, Zavala et al. (2022) measured velocities in those regions (see Figure 6.2). One of the observations was in H $\alpha$ , and it passes through several of the globule groups identified in this work.

In Figure 6.3 the globule groups lie along an ellipse, indicating that they are on a spherical shell<sup>2</sup>. In slit H, the shell radius can be read off the vertical axis (position). In the same slit, using the horizontal axis (velocity), we see that all these shells have a velocity of  $40\text{ km s}^{-1}$ . In this way we obtain the true separation between the globules and the star. Thus, combining the projected separation measured directly from the images with the true separation derived from the slit spectra, we can infer the inclination angle.

<sup>1</sup>Since we are estimating only the masses of the globules, not of their shells, we include all 168 identified globules.

<sup>2</sup>See Appendix I for additional details.

Figure 6.4 shows that our inclination estimates (red points), obtained by comparing the shell pressure with the external wind pressure (Section 5.2), agree with the independent estimates from two-dimensional spectra (blue points) (Henney, W., in prep.). The two determinations are fully independent, and we see a clear anti-correlation between inclination angle and observed separation. In this plot we do not expect globules with inclination angles of  $\pm 90^\circ$ , because such globules would lie directly in front of or behind the star and would not be visible: in projection they would be too close to the WR star and strongly affected by its emission.

The nearest group of globules to the star appears to lie at about  $15''$  (0.39 pc) in Figure 6.3, consistent with our measurements in Figure 5.6. The latter also shows that many globules have true separations near  $18''$  (0.47 pc).

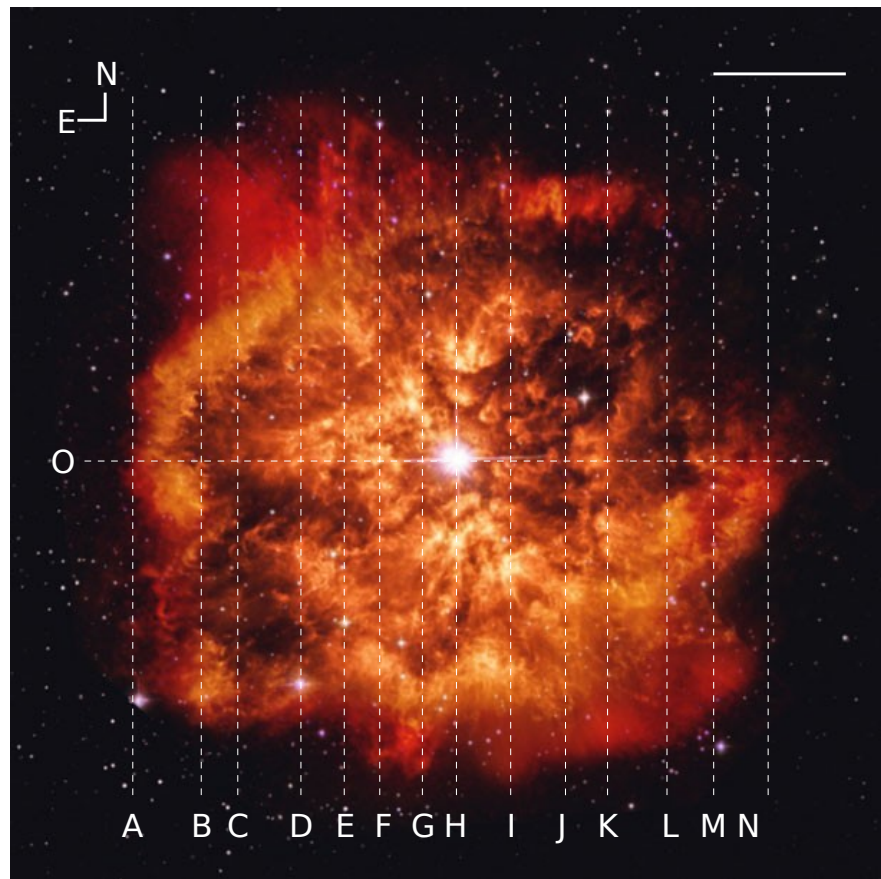


Figure 6.2: Dashed lines mark the positions where Zavala et al. (2022) obtained long-slit spectroscopy of the M1-67 nebula. These observations were made at San Pedro Mártir. The solid line in the upper-right corner corresponds to  $20''$ .

In Figure 6.3 we see that most globule groups are redshifted, with only a few blueshifted. That is, most of the groups sampled by these slits are receding from us, while only a few are approaching.

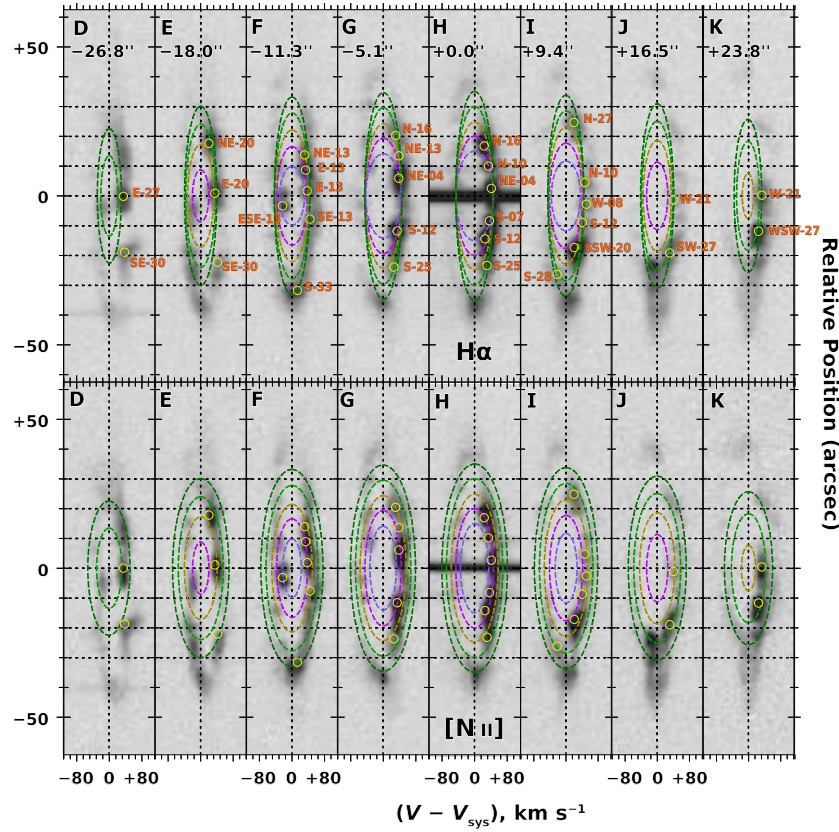


Figure 6.3: Long-slit spectroscopy from Zavala et al. (2022). Top:  $\text{H}\alpha$  emission; bottom:  $[\text{N II}]$  emission. Yellow circles mark the positions of globule groups intersected by each slit. Ellipses show spherical-shell models with radii of  $15''$  (purple),  $20''$  (pink),  $25''$  (yellow),  $30''$  (light green), and  $35''$  (green), all with expansion velocity  $40 \text{ km s}^{-1}$ .

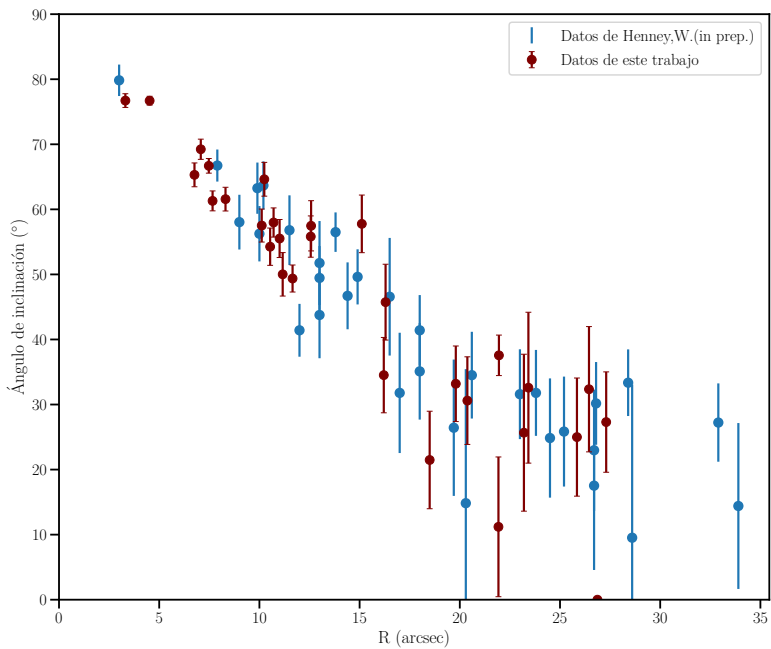


Figure 6.4: Red points: our inclination-angle estimates from Section 5.2, where the shell pressure is assumed to be in equilibrium with the external wind pressure. Blue points: inclination-angle estimates derived from the two-dimensional spectra of Zavala et al. (2022).

# Chapter 7

## Conclusions

In this thesis we have proposed a stationary hydrodynamic model to explain the interaction between the photoevaporative flows from the globules in the M1-67 nebula and the stellar wind from the WR 124 star.

The globules, as well as their shocked shells, were detected thanks to a range of observations. From these observations it was possible to determine several physical parameters by fitting two Gaussians plus a constant, as described in Chapter 4. The derived physical parameters were:

- Projected separation between globule and star
- Radius of the globules
- Radius of the shell
- Width of the shocked shell
- Brightness of the globule
- Brightness of the shell

Using the emission measure (EM), we calculated the density in the shocked shell (Section 4.3), and, assuming that the shocked shell is dominated by thermal pressure, we were able to determine the shell pressures of the globules.

In Figure 5.2 we saw that the pressure in the globules is lower than the ram pressure of the stellar wind. However, by introducing an inclination angle with respect to the plane of the sky, we could achieve pressure equilibrium between the shell pressure and the stellar-wind ram pressure (Figure 5.4). These inclination estimates, derived under the assumption of pressure equilibrium (Section 5.2), are consistent with the independent measurements obtained from two-dimensional spectra (Section 6.3).

Furthermore, using HST observations we compared the ratio of the thermal pressure in the shell to that of the photoevaporative flow at the base of the globule (Section 5.1). These measurements agree well with our theoretical model, as shown in Figure 5.1.

We can therefore conclude that this simple model provides a good description of the interaction between the photoevaporative flows of the globules and the stellar wind of WR 124. The model contains no free parameters, and its consistency with other studies strengthens our proposed scenario. This supports our assumptions that the globules have already passed through the phases described in Chapter 1 and that they are now in ionization equilibrium.

Although the model was originally formulated for a simple scenario of a globule irradiated by a single source, it could be extended to situations where multiple sources irradiate the globule, with one of them dominating the ionizing photon flux.

## Appendix A

# Filtros de las observaciones

En este apéndice vamos a dar más detalles acerca de los diferentes filtros que se utilizaron en las observaciones.

### A.1 Filtro del HST

Para el caso del HST solo se utilizaron las observaciones del filtro f656n, en el cual podemos ver la emisión de H $\alpha$ . Este filtro observa desde 6548.77 Å hasta 6674.27 Å y está centrada en 6563.8 Å como se puede ver en la Figura A.1.

### A.2 Filtros del JWST

Para el caso de las observaciones del JWST se utilizaron diferentes filtros, tanto del NIRcam como del MIRI. El filtro f1130w es el único filtro del MIRI y observa desde 10.953–11.667  $\mu\text{m}$  y está centrado en 11.3  $\mu\text{m}$ . En la Figura A.2 vemos la transmisión de este filtro.

Para los filtros del NIRcam tenemos a los filtros f090w, f150w, f444w, f210m y f335m, en la tabla A.1 podemos ver en qué longitudes de onda observa cada filtro. En la Figura A.3 vemos la transmisión de cada filtro.

En el filtro f090w podemos ver algunas líneas de emisión como [SIII] en las longitudes de onda de .906 y .935  $\mu\text{m}$ , así como una línea de la serie de Paschen de H $\text{I}$  en la longitud de onda de .954  $\mu\text{m}$ . En el filtro f150w se puede ver líneas de emisión de HeI en las longitudes de onda de 1.34 y 1.5  $\mu\text{m}$ , así como una línea de la serie de Brackett de H $\text{I}$  en la longitud de onda de 1.64  $\mu\text{m}$ . En el filtro f210m podemos encontrar líneas de emisión como las de HeI en la longitud de onda de 2.05  $\mu\text{m}$ , una línea de H $_2$  en la longitud de onda de 2.12  $\mu\text{m}$  y una línea de la serie de Brackett de H $\text{I}$  en la longitud de onda de 2.16  $\mu\text{m}$ . En el filtro f333m podemos ver líneas de emisión de PAHs en la longitud de onda de 3.3  $\mu\text{m}$ , una línea de la serie Pfund de H $\text{I}$  en la longitud de onda de 3.29  $\mu\text{m}$  y una línea de HeI en la longitud de onda de 3.36  $\mu\text{m}$ . En el filtro f444w podemos encontrar líneas de emisión de H $\text{I}$  en las longitudes de onda de 4.05 y 4.65  $\mu\text{m}$ ,

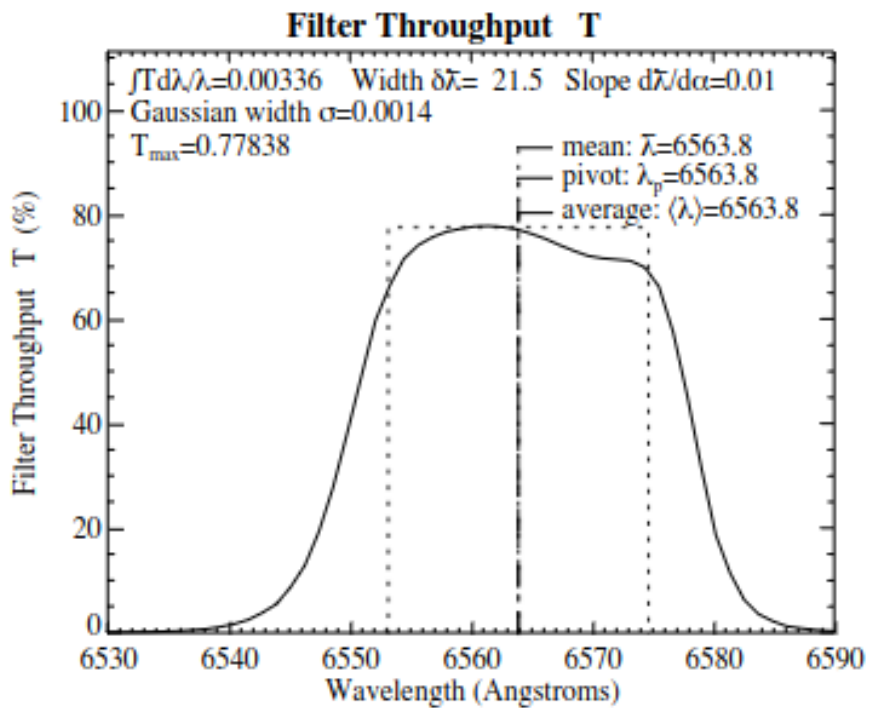


Figure A.1: Transmisión del filtro f656n del HST

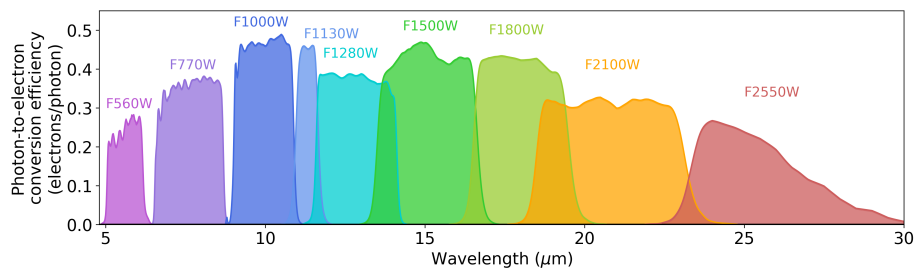


Figure A.2: Transmisión de los filtros de MIRI. El filtro f1130w está en azul.

así como una línea de emisión de [MgIV] en la longitud de onda de  $4.48 \mu\text{m}$ . Estas son algunas líneas de emisión que se pueden encontrar en los diferentes filtros de acuerdo a la literatura.

filtro	$\lambda_0(\mu\text{m})$	$\lambda_{min}(\mu\text{m})$	$\lambda_{max}(\mu\text{m})$
f090w	.903	.795	1.005
f150w	1.501	1.331	1.668
f210m	2.096	1.992	2.201
f335m	3.362	3.177	3.537
f444w	4.401	3.880	4.981

Table A.1: Rango en el que observa cada filtro utilizado para las observaciones utilizadas.  $\lambda_0$  es la longitud de onda a la que está centrado cada filtro,  $\lambda_{min}$  es la longitud de onda mínima a la que observa y  $\lambda_{max}$  es la longitud de onda más grande a la que observa cada filtro.

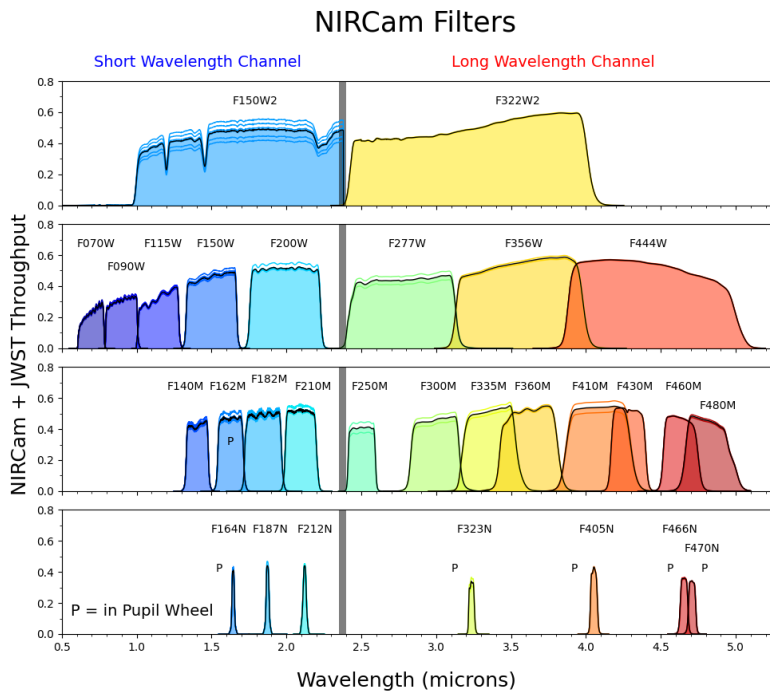


Figure A.3: Transmisión de los filtros de NIRcam. Los filtros f090w, f150w y f444w se encuentra en la segunda imagen, mientras que los filtros f210m y f335m se encuentran en la tercera imagen.

## Appendix B

# Estimación de fuerzas en el flujo fotoevaporativo ionizado

En estas estimaciones de las diferentes fuerzas solo haremos aproximaciones, por lo que para los cálculos vamos a usar los valores típicos de los ajustes (tabla 4.1 y 5.1).

Para comparar las distintas fuerzas es más conveniente comparar las presiones o aceleraciones ya que estas son fuerza por unidad de área o fuerza por unidad de masa, respectivamente.

Primero vamos a considerar la aceleración provocada por el gradiente de presión, para esto tomamos la fuerza por unidad de masa la cual está dada por

$$\rho a = \frac{dP}{dr} \Rightarrow a = \frac{1}{\rho} \frac{dP}{dr} = \frac{1}{\rho} \frac{\partial \rho}{\partial r} \frac{\partial P}{\partial \rho} = \frac{c_s^2}{h} \quad (\text{B.1})$$

como estamos considerando un gas isotérmico, vemos que del lado derecho tenemos los factores de la velocidad del sonido cuadrada y la escala de altura  $h$ , la cual está definida por

$$h^{-1} = \left| \frac{1}{\rho_0} \frac{\partial \rho}{\partial r} \right| = \left| \frac{d \ln \rho}{dr} \right| \quad (\text{B.2})$$

usando las ecuaciones (2.7) y (2.9) tenemos que

$$\frac{\rho}{\rho_0} = e^{\frac{1-M^2}{2}} \Rightarrow \ln \frac{\rho}{\rho_0} = \frac{1-M^2}{2} \quad (\text{B.3})$$

$$\Rightarrow d \ln \frac{\rho}{\rho_0} = -M dM \quad (\text{B.4})$$

por otro lado usando que

$$\frac{r}{r_0} = M^{-1/2} e^{\frac{M^2-1}{2}} \quad (\text{B.5})$$

tenemos que

$$d \frac{r}{r_0} = e^{\frac{M^2-1}{4}} \left( -\frac{M^{-3/2}}{2} + \frac{M}{2M^{1/2}} \right) dM = \frac{e^{\frac{M^2-1}{4}}}{2} \left( M^{1/2} (1 - 1/M^2) \right) dM \quad (\text{B.6})$$

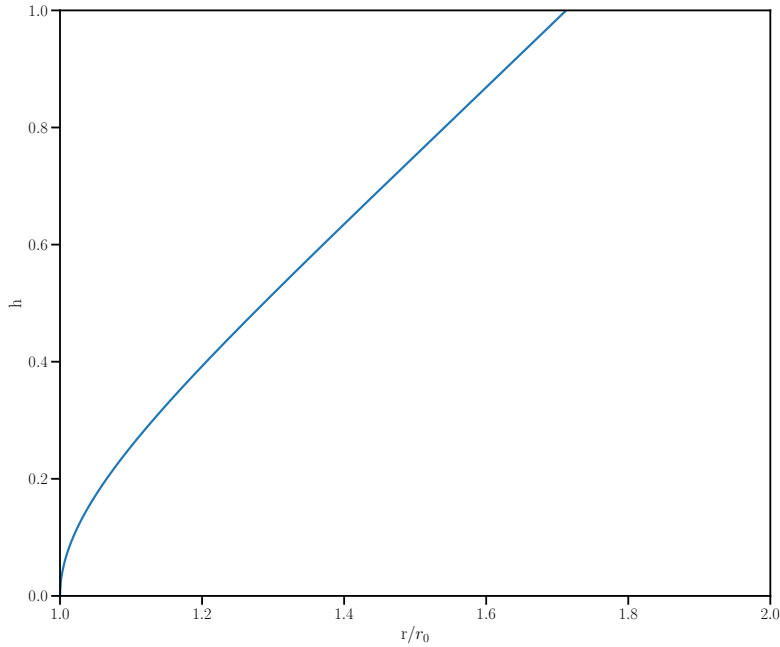


Figure B.1: Gráfica de  $h$  con respecto al radio normalizado. Vemos que cerca de donde tenemos la emisión en  $r/r_0$  el valor de  $h$  es del orden de 0.1

por lo que

$$h^{-1} = \left| \frac{2M}{e^{\frac{M^2-1}{4}} (M^{1/2} - M^{-3/2})} \right| \quad (\text{B.7})$$

que como podemos ver en la Figura B.1 cuando  $r/r_0 \sim 1$  tenemos un valor del orden de  $0.2^1$ . Por lo que el gradiente de presión nos da una aceleración de

$$a_p \approx \frac{c_s^2}{0.2r_0} = 3.8 \times 10^{-4} \text{ cm s}^{-2} \quad (\text{B.8})$$

a un radio típico  $r_0 \sim 0.135''$ . Como el modelo se resolvió en el eje de simetría, tenemos que aquí los gradientes transversales son cero, mientras que si consideramos el modelo a cierto ángulo debemos considerar que el gradiente de densidad transversal es más pequeño, por un factor de 10 aproximadamente.

---

<sup>1</sup>En la Figura B.1 vemos que cuando  $r = r_0$   $h \rightarrow 0$ , por lo que tendríamos una aceleración infinita.

## B.1 Fuerzas de gravedad

Hamann, W.-R. et al. (2019) estima una masa de  $20\text{--}22 M_{\odot}$  para la estrella WR 124, por lo que la fuerza de gravedad por parte de la estrella nos da un aceleración de

$$a_* = \frac{GM_*}{R^2} \approx 1.97 \times 10^{-9} \text{ cm/s}^2 \quad (\text{B.9})$$

con  $R$  una distancia típica entre la estrella y el glóbulo de  $14.96''$ . Si tomamos la distancia típica considerando el ángulo de inclinación  $i$  (Sección 5.2), vemos que esta aceleración es todavía más pequeña.

Ahora vamos a considerar la aceleración por parte de la gravedad del mismo glóbulo. Para esto, vamos a considerar la masa neutra del glóbulo y la masa ionizada. En la sección 6.2 hablamos de como obtener la masa neutra de los glóbulos, para la masa ionizada vamos a considerar la masa que se encuentra en la mitad de la cáscara que hay entre  $r_0$  y  $r_{\text{shell}}$ , por lo que a masa ionizada es

$$M_i = \rho_1 \frac{2\pi}{3} (r_{\text{shell}}^3 - r_0^3) \quad (\text{B.10})$$

donde  $\rho_1$  es la densidad por unidad de masa en la parte ionizada. De esta manera, tenemos que la masa del glóbulo a es  $M_g = M_i + M_n \approx 7.87 \times 10^{-4} M_{\odot}$  (considerando una  $v_A = 1 \text{ km s}^{-1}$  para la parte neutra) y la aceleración por parte de la fuerza de gravedad del mismo glóbulo es de

$$a_g = \frac{GM_g}{r_{\text{shell}}^2} \approx 4.55 \times 10^{-11} \text{ cm/s}^2. \quad (\text{B.11})$$

Si en esta estimación tomamos una  $v_A$  mayor, tendríamos una aceleración un poco menor. De igual, si consideramos la densidad ionizada de la tabla 5.1, esta aceleración no cambia mucho. Para el caso de los glóbulos que están en grupo, de igual manera podemos despreciar la aceleración por parte de los demás glóbulos, ya que por muy cercanos que estén, podemos considerar una distancia mínima de  $r_{\text{shell}}$ .

De esta manera tenemos que

$$a_g < a_* \ll a_p \quad (\text{B.12})$$

donde  $a_g$  es la aceleración provocada por la gravedad del glóbulo,  $a_*$  la aceleración provocada por la estrella WR 124 y  $a_p$  la aceleración provocada por la diferencia de presiones en la superficie del glóbulo.

## B.2 Presión de radiación

Vamos a considerar la presión de radiación ya que podemos suponer que todo el momento de los fotones ionizantes se va al flujo photoevaporativo, por lo que si consideramos que todo la radiación ionizante es absorbida en el flujo photoevaporativo entonces tenemos que para la radiación ionizante  $Q = 1.25 \times 10^{49} \text{ s}^{-1}$ ,

según la tabla 1.1, tendríamos una intensidad de

$$\frac{Qh\nu}{4\pi R^2} = \frac{2.74 \times 10^{38} \text{ erg s}^{-1}}{4\pi R^2} \approx 6.8 \text{ erg s}^{-1} \text{ cm}^{-2} \quad (\text{B.13})$$

para la frecuencia que corresponde a 1 Ry, el cual es un límite inferior para los fotones que son capaces de ionizar el gas neutro, esto a una distancia típica de los glóbulos. Por lo que tendríamos una presión de radiación de  $P_r \approx 2.26 \times 10^{-10} \text{ dyn cm}^{-2} < P_{\text{shell}}$ .

A pesar de que consideramos que el glóbulo esta soportado principalmente por un campo magnético, no vamos a considerar presión magnética en el gas ionizado ya que este sería despreciable con la presión térmica (Henney et al., 2009).

## Appendix C

# Predicciones del modelo fotoevaporativo para la densidad ionizada en el frente de ionización

En el modelo suponemos un estado estacionario y además, también suponemos que no hay absorción por polvo, por lo que el flujo incidente de fotones,  $F_0$ , debe ser igual a la suma de dos términos, las recombinaciones por unidad de área y las nuevas ionizaciones

$$F_0 = n_{i,0} u_{i,0} + \int n^2 \alpha_B dr = n_{i,0} u_{i,0} + n_{i,0}^2 h_1 \alpha_B \quad (\text{C.1})$$

donde  $F_0$  es la tasa de fotones ionizantes por unida de área,  $n_{i,0}$  la densidad del gas ionizado,  $u_0$  la velocidad del gas ionizado y  $h_1$  es la anchura efectiva de la capa ionizada que se define como

$$n_0^2 h_1 = \int n^2 dr, \quad (\text{C.2})$$

el cual se puede estimar usando las ecuaciones (2.6), (2.7) y (2.9). Por lo que tendríamos que

$$h_1 = \int_0^\infty \left( \frac{n(r)}{n_0} \right)^2 dr = r_0 \int_1^\infty \frac{\exp(\frac{3}{4}(1 - M^2))}{2} (M^{1/2} - M^{3/2}) dM \approx 0.12r_0. \quad (\text{C.3})$$

Tomando los valores de  $F_0$  y  $r_0$  de nuestros glóbulos, tenemos que, el primer término del lado derecho de la Ecuación (C.1) es muy pequeño en comparación con el segundo término. Por lo que podemos despreciar este término.

74 APPENDIX C. DENSIDAD IONIZADA EN EL FRENTE DE IONIZACIÓN

## Appendix D

# Combos de filtros

En este apéndice vamos a explicar como se obtuvieron los combos de gas ionizado y gas neutro utilizando las diferentes observaciones del JWST. Usamos estas combinaciones para hacer ajustes a los perfiles de brillo y así obtener mediciones del radio del glóbulo, de la cáscara chocada y su ancho.

Como usamos diferentes filtros, los cuales tienen diferente resolución, hicimos una convolución para que todos tuvieran la misma resolución y así poder combinar imágenes. En este caso convolucionamos las imágenes para tener la misma resolución que el filtro f444w, el cual tiene la menor resolución de los filtros usados. Una vez que todas las imágenes tienen la misma resolución, normalizamos la emisión de las estrellas, el gas ionizado y PAHs a la emisión en el filtro f210m de sus respectivos mecanismos de emisión como se puede ver en la Tabla D.1. Como estos cocientes de imágenes se realizaron visualmente, tomamos el error como el rango completo en donde se encontraban estos cocientes.

Filtro	Estrellas	Gas ionizado	PAHs
f090w	$0.4 \pm 0.15$	$0.57 \pm 0.05$	$0.4 \pm 0.3$
f150w	$1.1 \pm 0.1$	$0.6 \pm 0.05$	$0.6 \pm 0.3$
f210m	1.0	1.0	1.0
f335m	$0.25 \pm 0.05$	$0.95 \pm 0.15$	$7.0 \pm 0.4$
f444w	$0.19 \pm 0.07$	$1.9 \pm 0.5$	$3.0 \pm 1.0$

Table D.1: Emisión de los diferentes componentes normalizados al filtro f210m.

De la Tabla D.1 podemos observar que la emisión de gas ionizado y PAHs en el filtro f150w es igual, por lo que con una simple combinación podemos tener solo la emisión de las estrellas como se puede ver en la Tabla D.2. Combinando los filtro f335m y f210m se pudo quitar la emisión de gas ionizado, de manera similar, combinando los filtros f444w y f335m quitamos la emisión de los PAHs (ver Tabla D.2).

Con la primer combinación de la Tabla D.2 podemos quitar la emisión de

	Combinación	Estrellas	Gas ionizado	PAHs
A	f150w – 0.6 f210m	$0.5 \pm 0.1$	$0.00 \pm 0.05$	$0.00 \pm 0.30$
B	f335m – 0.95 f210m	$-0.70 \pm 0.05$	$0.00 \pm 0.15$	$6.05 \pm 0.40$
C	f444w – 0.43 f335m	$0.08 \pm 0.07$	$1.49 \pm 0.50$	$-0.01 \pm 1.01$

Table D.2: Primera combinación de filtros.

las estrellas en las otras combinaciones y así poder ver solo la emisión de gas ionizado o de PAHs. En la primer combinación de la Tabla D.3 vemos solo la emisión de gas neutro y en la segunda combinación vemos solo la emisión de gas ionizado.

Combinación	Estrellas	Gas ionizado	PAHs
$1.4A + B$	$0.00 \pm 0.15$	$0.00 \pm 0.17$	$6.05 \pm 0.58$
$C - 0.16A$	$0.00 \pm 0.07$	$1.49 \pm 0.50$	$-0.01 \pm 1.01$

Table D.3: Combinación de filtros para ver solo la emisión de gas ionizado y PAHs.

## Appendix E

### Errores en $r_{\text{shell}}$ y $H_s$

Si consideramos que cada medición realizada en el gas ionizado en el JWST ,  $x_J^i$ , y que cada medición en en H $\alpha$  en el HST,  $x_H^i$ , lo podemos ver como la medición real más un error, es decir,

$$x_J^i = x + \epsilon_J^i, \quad x_H^i = x + \epsilon_H^i \quad (\text{E.1})$$

donde  $x$  es la medición real y que  $\epsilon_J^i$ ,  $\epsilon_H^i$  son respectivamente los errores en las mediciones de los dos telescopios. Entonces tenemos que

$$x_J^i - x_H^i = \epsilon_J^i - \epsilon_H^i, \quad (\text{E.2})$$

donde estamos considerando que los errores en los dos telescopios son independientes. Considerando que la varianza sobre toda la muestra está dada como

$$\text{Var}(x_J - x_H) = \frac{\sum_{i=1}^N ((x_J^i - x_H^i) - \mu)^2}{N} \quad (\text{E.3})$$

donde  $N$  es el tamaño de la muestra y  $\mu = N^{-1} \sum_{i=1}^N (x_J^i - x_H^i)$  es la media. Si las distribuciones son simétricas, esperamos que  $\mu \approx 0$  para  $N$  grande, esto fue verificado para nuestras muestras. Entonces, suponiendo que no hay correlación entre los errores  $\epsilon_J^i$  y  $\epsilon_H^i$ , tenemos que

$$\text{Var}(x_J - x_H) = \text{Var}(\epsilon_J) + \text{Var}(\epsilon_H) = \sigma_J^2 + \sigma_H^2, \quad (\text{E.4})$$

donde  $\sigma_J$  y  $\sigma_H$  son los promedios RMS de los errores en las mediciones. Si además suponemos que  $\sigma_J = \sigma_H \equiv \sigma$ , tenemos que  $\text{Var}(x_J - x_H) = 2\sigma^2 \Rightarrow \sigma = \sqrt{\text{Var}(x_J - x_H)/2}$ , el cual usamos como el estimado del incertidumbre en estas mediciones en la Sección 4.2.1.



## Appendix F

# Constante de conversión en las observaciones del HST

En este Apéndice vamos a justificar la constante de conversión para pasar de unidades del telescopio, cuentas  $\text{s}^{-1} \text{pix}^{-1}$ , a unidades físicas de brillo superficial,  $\text{erg cm}^{-2} \text{s}^{-1} \text{sr}^{-1}$ , en las observaciones de  $\text{H}\alpha$  en el HST. Para esto vamos a utilizar la calibración de Grosdidier et al. (1998) en la cual calculó un flujo total de la nebulosa de  $2.08 \times 10^{-10} \text{ erg s}^{-1} \text{cm}^{-2}$  en las observaciones de  $\text{H}\alpha$  en el HST. En esta calibración quita la contaminación de la línea  $[\text{NII}] \lambda 6548$  y del continuo. Por otro lado, calculamos un flujo en unidades del telescopio al sumar las cuentas de todos los píxeles de la nebulosa, después de aplicar una máscara para eliminar la contribución de las estrellas, teniendo un valor de 64 822.82 cuentas  $\text{s}^{-1}$ . Esta máscara toma en cuenta a los píxeles que se encuentra a una distancia mínima de  $1''$  y a una distancia máxima de  $60''$  de la estrella WR 124, así no estamos considerando la emisión por parte de la estrella, de igual manera, no sumamos los píxeles que tuvieran un valor mayor a 3 para no incluir la emisión de las estrellas de campo. Además, tomamos en cuenta el tamaño del píxel de  $0.1'' \times 0.1'' = 2.34 \times 10^{-13} \text{ sr}$ . Por lo que nuestro factor de conversión está dado como

$$\begin{aligned} 1 \text{ cuenta s}^{-1} \text{ pix}^{-1} &= \frac{2.08 \times 10^{-10}}{64822.82 \times 2.34 \times 10^{-13}} \text{ erg cm}^{-2} \text{s}^{-1} \text{sr}^{-1} \\ &\approx 0.0137 \text{ erg cm}^{-2} \text{s}^{-1} \text{sr}^{-1}. \end{aligned} \tag{F.1}$$



## Appendix G

# Corrección en la estimación de los brillos

En la Sección 5.1 usamos los resultados obtenidos a partir de las observaciones para comparar con el modelo. Por lo que ahora vamos a calcular las correcciones a los brillos estimados, tanto de la parte interna como de la cáscara, por efectos instrumentales.

En el caso de la cáscara, vamos a ignorar estas correcciones debido a que está bien resuelta y el brillo no se ve reducido por el PSF del telescopio.

Por otro lado, para la parte interna tenemos un radio muy pequeño. De hecho es casi un píxel en las observaciones del HST. Así que para esta corrección vamos a considerar dos efectos instrumentales, uno por el efecto del PSF y el otro por el tamaño del píxel.

Si asumimos que el perfil de brillo real tiene un perfil gaussiano como función de la distancia  $r$

$$B(r) = B_0 e^{-r^2/2\sigma_0} \quad (\text{G.1})$$

tenemos que el flujo total está dado como

$$F_0 = \iint_{-\infty}^{\infty} B(r) dx dy = B_0 \pi r_{\text{eff}}^2 = B_0 2\pi \sigma_0^2. \quad (\text{G.2})$$

Para considerar estas correcciones por los dos efectos instrumentales, vamos a asumir que estos también están dados por perfiles gaussianos. De este modo, al convolucionar dos perfiles gaussianos con parámetros  $\sigma_1$  y  $\sigma_2$ , tenemos que

$$\sigma^2 = \sigma_1^2 + \sigma_2^2 \quad (\text{G.3})$$

donde  $\sigma$  sería el parámetro de los dos perfiles convolucionados.

En nuestro caso, lo que observamos es el perfil del brillo real convolucionado con el perfil del PSF y el perfil de las rendijas de los píxeles. Entonces

$$\sigma_{\text{obs}}^2 = \sigma_0^2 + \sigma_{\text{PSF}}^2 + \sigma_{\text{pix}}^2 \quad (\text{G.4})$$

## 82 APPENDIX G. CORRECCIÓN EN LA ESTIMACIÓN DE LOS BRILLOS

donde  $\sigma_{\text{PSF}} = \frac{W_{\text{PSF}}}{2\sqrt{2 \ln 2}}$ , siendo  $W_{\text{PSF}}$  el ancho del PSF a la altura media, y  $\sigma_{\text{pix}} = \frac{\Delta X_{\text{pix}}}{\sqrt{2\pi}}$ , siendo  $\Delta X_{\text{pix}}$  el tamaño del píxel. Entonces, para comparar el los brillos reales y los observados tenemos que

$$\frac{F_0}{F_{\text{obs}}} = \frac{B_0 \sigma_0^2}{B_{\text{obs}} \sigma_{\text{obs}}^2} = \frac{B_0}{B_{\text{obs}}} \frac{\sigma_0^2}{\sigma_0^2 + \sigma_{\text{PSF}}^2 + \sigma_{\text{pix}}^2} \quad (\text{G.5})$$

$$\Rightarrow \frac{B_0}{B_{\text{obs}}} = 1 + \frac{\sigma_{\text{PSF}}^2 + \sigma_{\text{pix}}^2}{\sigma_0^2}. \quad (\text{G.6})$$

Debido a que usamos un solo radio para todos los glóbulos, esta corrección es solo una constante, y gracias a este valor, los datos obtenidos a partir de las observaciones se ajustan muy bien al modelo propuesto.

# Appendix H

## Escalas de tiempo

### H.1 Tiempo dinámico

Usando los valores de la tabla 4.1, para el flujo fotoevaporativo tenemos un tiempo dinámico

$$t_{\text{DF}} = \frac{r_{\text{shell}}}{v} = \frac{0.01 \text{ pc}}{10 \text{ km s}^{-1}} \approx 5.27 \times 10^{10} \text{ s} = 1.67 \times 10^3 \text{ a.} \quad (\text{H.1})$$

Marchenko et al. (2010) estima una velocidad de expansión para la nebulosa de  $42\text{--}46 \text{ km s}^{-1}$  por lo que para la nebulosa tenemos un tiempo dinámico de

$$t_{\text{DN}} = \frac{R_{\text{nebula}}}{v_{\text{exp}}} \approx \frac{1.5 \text{ pc}}{46 \text{ km s}^{-1}} = 1 \times 10^{12} \text{ s} = 3.18 \times 10^4 \text{ a} \quad (\text{H.2})$$

### H.2 Tiempo de recombinación

Usando la densidad promedio de la tabla 4.1 tenemos un tiempo de recombinación

$$t_{\text{r}} = \frac{1}{\alpha_B n} \approx 3.64 \times 10^9 \text{ s} = 115.64 \text{ a} \quad (\text{H.3})$$

Para el caso del tiempo de calentamiento-enfriamiento, vamos a considerar que es de 3–5 veces menor que el tiempo de recombinación. Esto considerando que  $t_c = \frac{3P}{2\mathcal{L}} = \frac{3k_B T}{\Lambda n}$  donde  $P = 2nk_B T$  es la presión y  $\mathcal{L} = \Lambda n^2$ , así tenemos que  $\frac{t_c}{t_{\text{r}}} = \frac{3k_B T \alpha_B}{\Lambda}$  y considerando que  $3k_B T \approx 4 \times 10^{-12} \text{ erg}$ ,  $\alpha_B = 2.6 \times 10^{-13} \text{ cm}^3 \text{ s}^{-1}$  y  $\Lambda \approx 3 \times 10^{-24} \text{ erg cm}^3 \text{ s}^{-1}$  entonces

$$\frac{t_c}{t_{\text{r}}} \approx \frac{10^{-24} \text{ erg cm}^3 \text{ s}^{-1}}{3 \times 10^{-24} \text{ erg cm}^3 \text{ s}^{-1}} = \frac{1}{3} \quad (\text{H.4})$$

### H.3 Tiempo de vida de los glóbulos

Para calcular el tiempo de vida de los glóbulos, primero vamos a considerar que su tasa de pérdida de masa está dada por

$$\dot{M} = \pi r_0^2 n_{i,0} c_{s,i} m_H \quad (\text{H.5})$$

usando los valores típicos de la tabla 4.1, tenemos que  $\dot{M} = 4.91 \times 10^{-8} M_\odot \text{ a}^{-1}$ . Por lo que el tiempo de vida de los glóbulos es

$$t_{\text{glo}} = \frac{M_g}{\dot{M}} = 9.16 \times 10^4 \text{ a} \quad (\text{H.6})$$

#### H.3.1 Comparación de las diferentes escalas de tiempo

De lo anterior, tenemos que

$$t_{\text{cool}} < t_r \ll t_{\text{DF}} \ll t_{\text{DN}} \sim t_{\text{glo}}. \quad (\text{H.7})$$

Con lo que podemos asumir un equilibrio de ionización/recombinación,, así como un equilibrio de calentamiento/enfriamiento dado que estos dos procesos micro físicos ocurren en un tiempo de escala mucho menor que los demás. También podemos justificar que el modelo propuesto es estacionario ya que este tienen una escala de tiempo mucho menor que la expansión de la nebulosa.

## Appendix I

# Proyección de posición y velocidad

En la Sección 6.3 analizamos las observaciones de rendija larga de los glóbulos para poder determinar su distribución tridimensional. A pesar de que no podemos medir directamente la posición a lo largo de la vista de visión, si suponemos que los glóbulos se alejan de la estrella WR 124 estrictamente de manera radial a una velocidad  $v(r)$ , podemos usar la velocidad observada a lo largo de la línea de visión para obtener esta componente espacial que nos falta.

Consideremos un glóbulo (o un grupo de glóbulos) con coordenadas cartesianas  $(x, y, z)$ , donde la estrella WR 124 se encuentra en el origen. En este análisis vamos a considerar que el eje  $y$  es paralelo a nuestra línea de visión, por lo que las posiciones en  $x$  y  $z$  son las posiciones en el plano del cielo, y las rendijas serán paralelas al eje  $z$ . Por simplicidad vamos a usar las coordenadas adimensionales  $X = x/r$ ,  $Y = y/r$  y  $Z = z/r$ , donde  $r = (x^2 + y^2 + z^2)^{1/2}$  es el radio. De esta manera, si suponemos que el vector de velocidad,  $(v_x, v_y, v_z)$ , es paralelo al vector de posición, entonces tenemos que  $X = v_x/v$ ,  $Y = v_y/v$  y  $Z = v_z/v$ , donde  $v = (v_x^2 + v_y^2 + v_z^2)^{1/2}$  es la magnitud de la velocidad. La cual estamos considerando únicamente como función del radio.

Considerando estas coordenadas adimensionales, en la Figura I.1 podemos ver la esfera unitaria

$$X^2 + Y^2 + Z^2 = 1 \quad (\text{I.1})$$

en el plano  $(X, Z)$ , el cual representa el plano del cielo en el que vemos, y nuestra línea de visión sería el eje  $Y$ , el cual apunta hacia adentro de la imagen. La línea azul paralela al eje  $Z$  representa una de las rendijas usadas por Zavala et al. (2022) en la nebulosa. Notemos que si está rendija se encuentra en  $X_0$ , podemos dibujar el círculo

$$Y^2 + Z^2 = 1 - X_0^2 \equiv \xi^2 \quad (\text{I.2})$$

en el plano paralelo a  $(Y, Z)$  que pasa por  $X_0$ , como se ve en la Figura I.2. Este círculo representa la posición de la elipse tanto en posición como en velocidad.

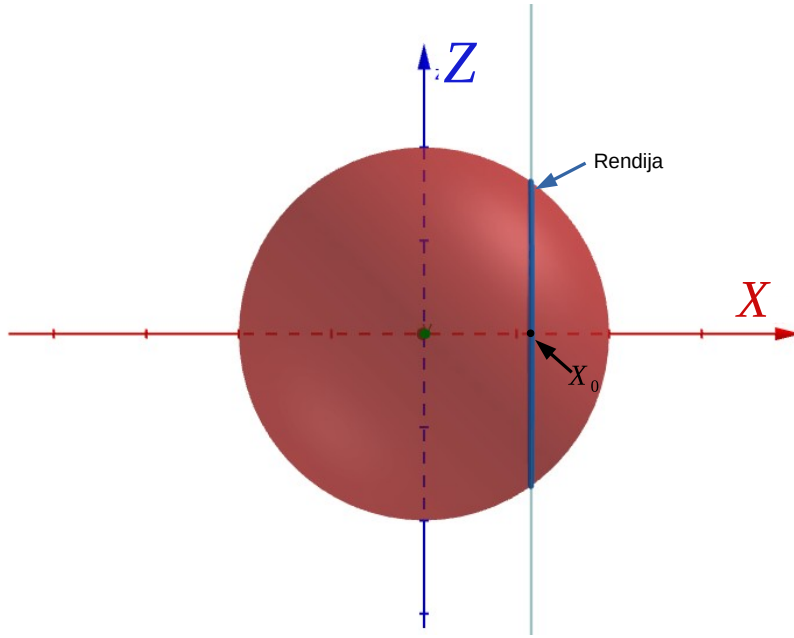


Figure I.1: Visualización de como se vería una rendija que pasa en  $X_0$  sobre la esfera unitaria. El plano  $(X, Z)$  representa el plano en el cielo y nuestra línea de visión va en dirección del eje  $Y$ , hacia adentro de la imagen.

Mientras que las elipses de la Figura 6.3 se caracterizan por los semi-ejes en coordenadas físicas  $\xi r$  en la dirección espacial a lo largo de la rendija y  $\xi v(r)$  en la velocidad a lo largo de la línea de visión. En la Sección 6.3 consideramos dos casos limitantes para la velocidad. Un caso con una velocidad constante  $v(r) = 46 \text{ km s}^{-1}$  y el caso donde la velocidad es proporcional al radio  $v(r) = 46 \text{ km} - \text{s}^{-1}(r/20'')$ . Por lo que, si tomamos  $Z = z/r$  y  $Y = v_y/v$  entonces el círculo dado por la Ecuación (I.2) representa las elipses de la Figura 6.3 pero normalizados.

Podemos observar también que el círculo  $Y^2 + Z^2 = 1 - X_0^2$  tiene un radio menor que la esfera unitaria para  $X_0 \neq 0$  (ver Figura I.3), por lo que entre más lejos este  $X_0$  del origen, el círculo se hace más pequeño. Es por eso que las elipses de la Figura 6.3 se van haciendo más pequeñas conforme la rendija usada en la que se encuentran está más alejada de la estrella WR 124.

Notemos que además que si  $Z = 0$ , entonces tenemos el máximo en  $Y$ , que es el radio del círculo  $\sqrt{1 - X_0^2}$ . De igual manera para el caso  $Y = 0$ . Estas proyecciones son usadas para la discusión en la Sección 6.3

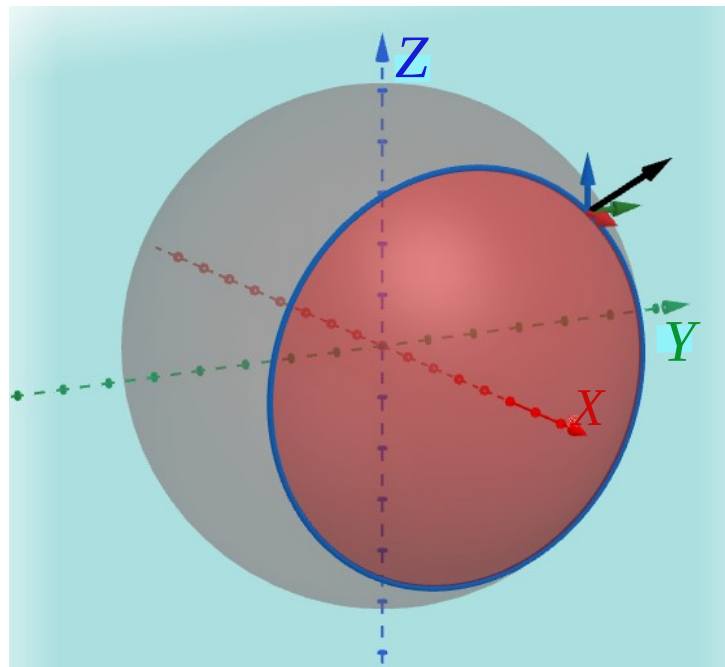


Figure I.2: El círculo  $Y^2 + Z^2 = 1 - X_0^2$  con centro en  $(0, 0, X_0)$  esta sobre un plano paralelo al plano  $(Y, Z)$ . La flecha negra indica el vector de posición, o de velocidad ya que los estamos tomando como paralelos, y las flechas de colores son sus proyecciones en sus respectivos ejes.

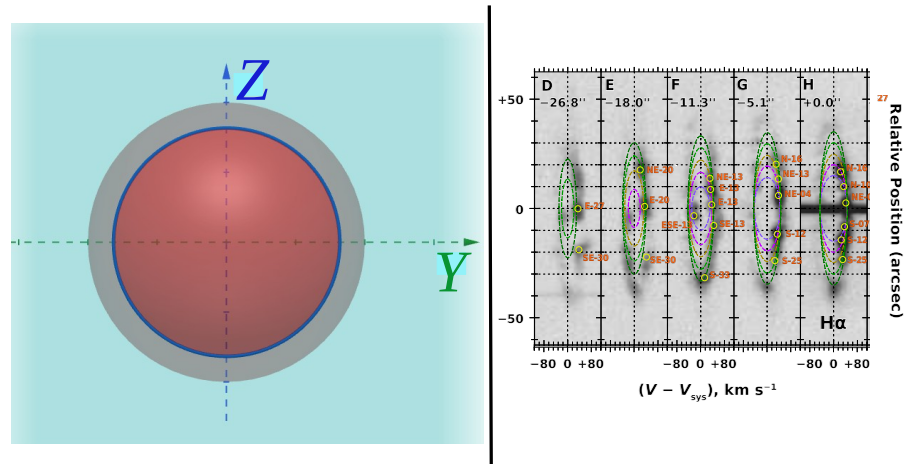


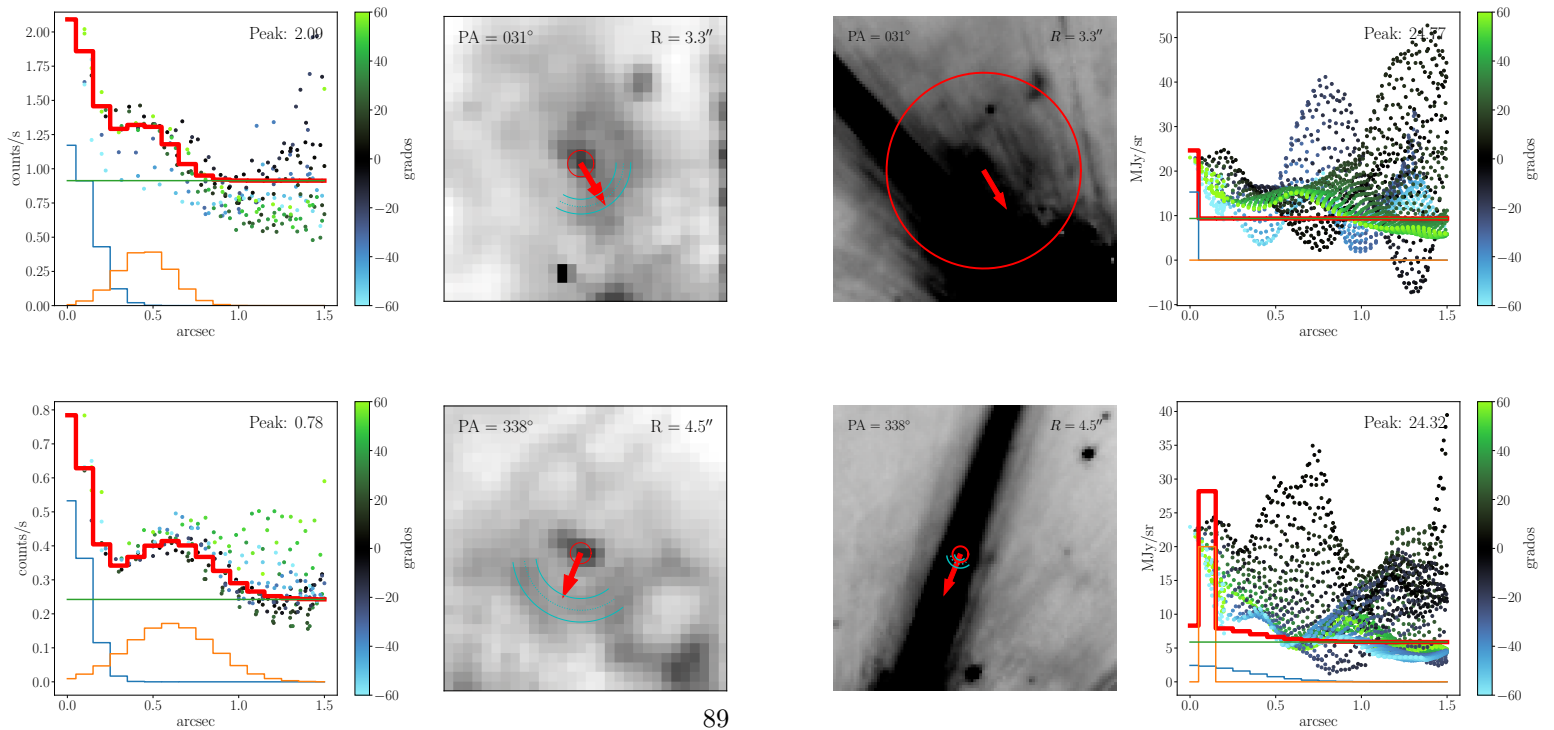
Figure I.3: En la imagen de la izquierda vemos como se vería el esquema de Posición-Velocidad con los ejes normalizados a un radio  $r$  y una velocidad  $v(r)$ , se puede apreciar que conforme  $X_0$  se aleja del origen, nuestro círculo se hace cada vez más pequeños. Es por eso que en la imagen de la derecha las elipses se hacen más pequeñas conforme las rendijas están más alejadas de la rendija H, que es la que pasa por la estrella.

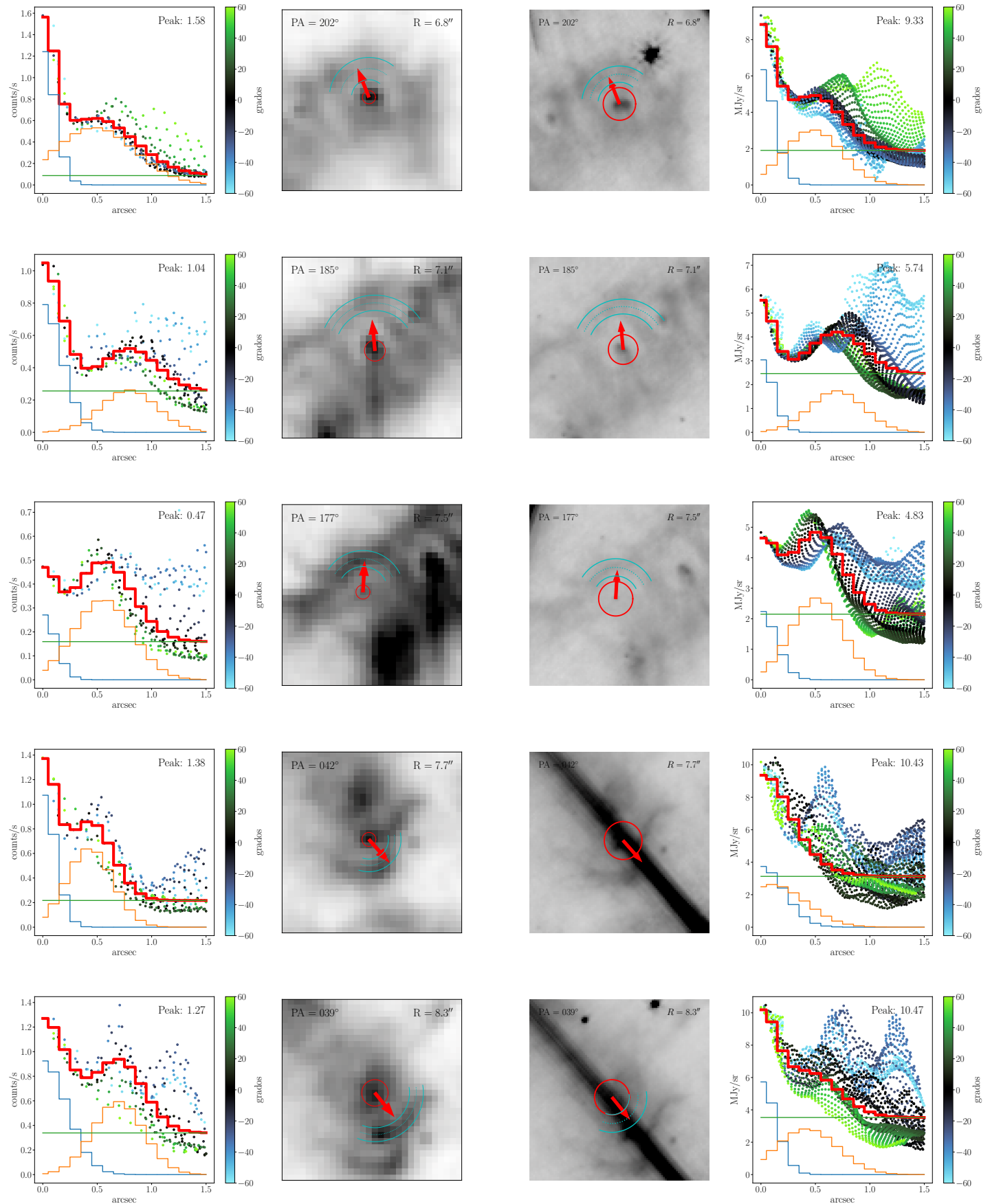
## Appendix J

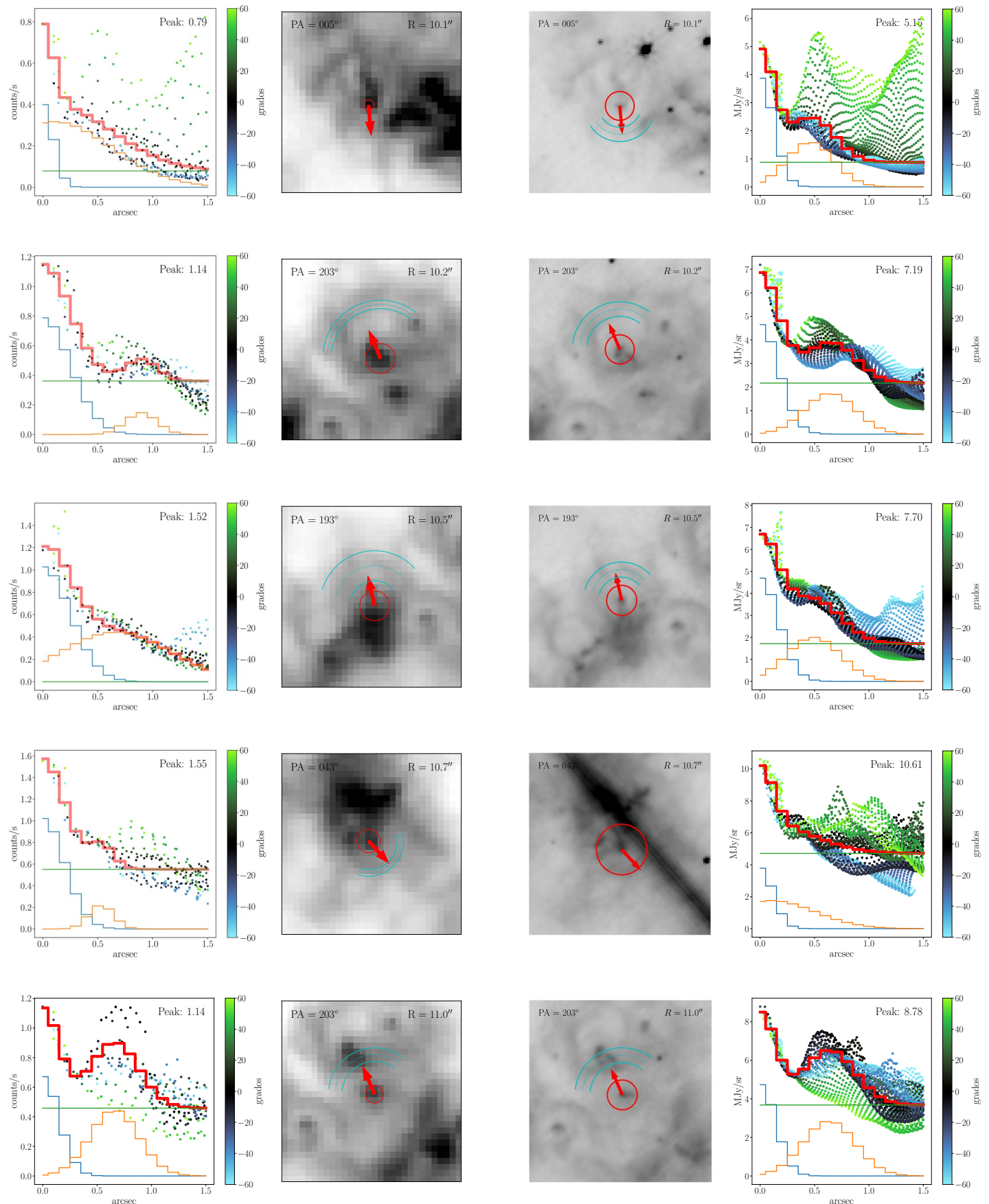
# Imágenes de ajustes

En este Apéndice mostramos los ajustes realizados a los glóbulos. En la parte izquierda mostramos el ajuste a los perfiles de brillo para las observaciones del HST y a su lado la visualización de estos ajustes en el filtro f656n del HST. Del lado derecho vemos el ajuste a los perfiles de brillo para el gas ionizado usando los datos del JWST, y a su lado la representación de estos ajustes en el filtro f090w del JWST, ya que morfológicamente se parece a las imágenes del HST.

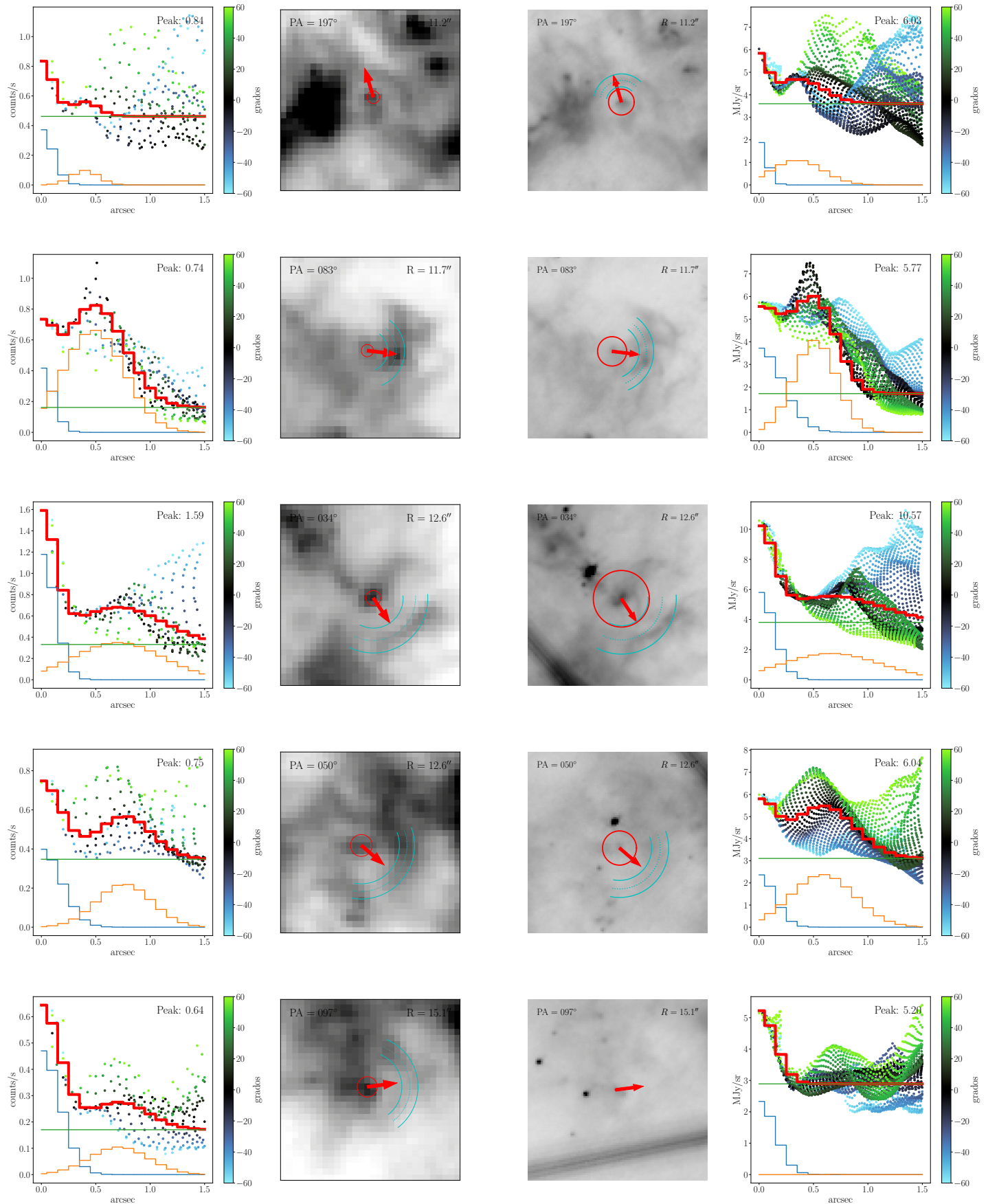
Figure J.1: Visualización de los ajustes realizados a los glóbulos.

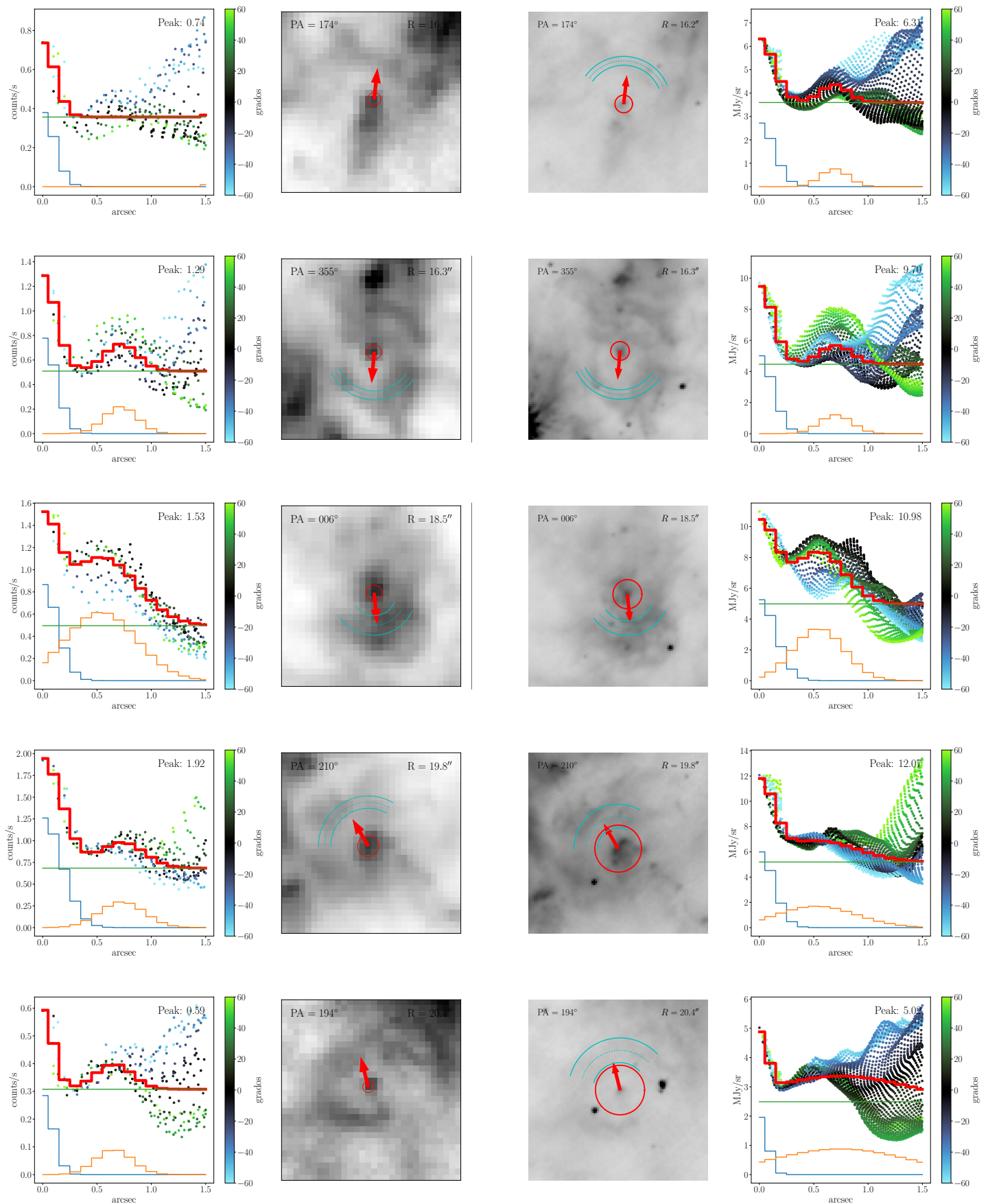




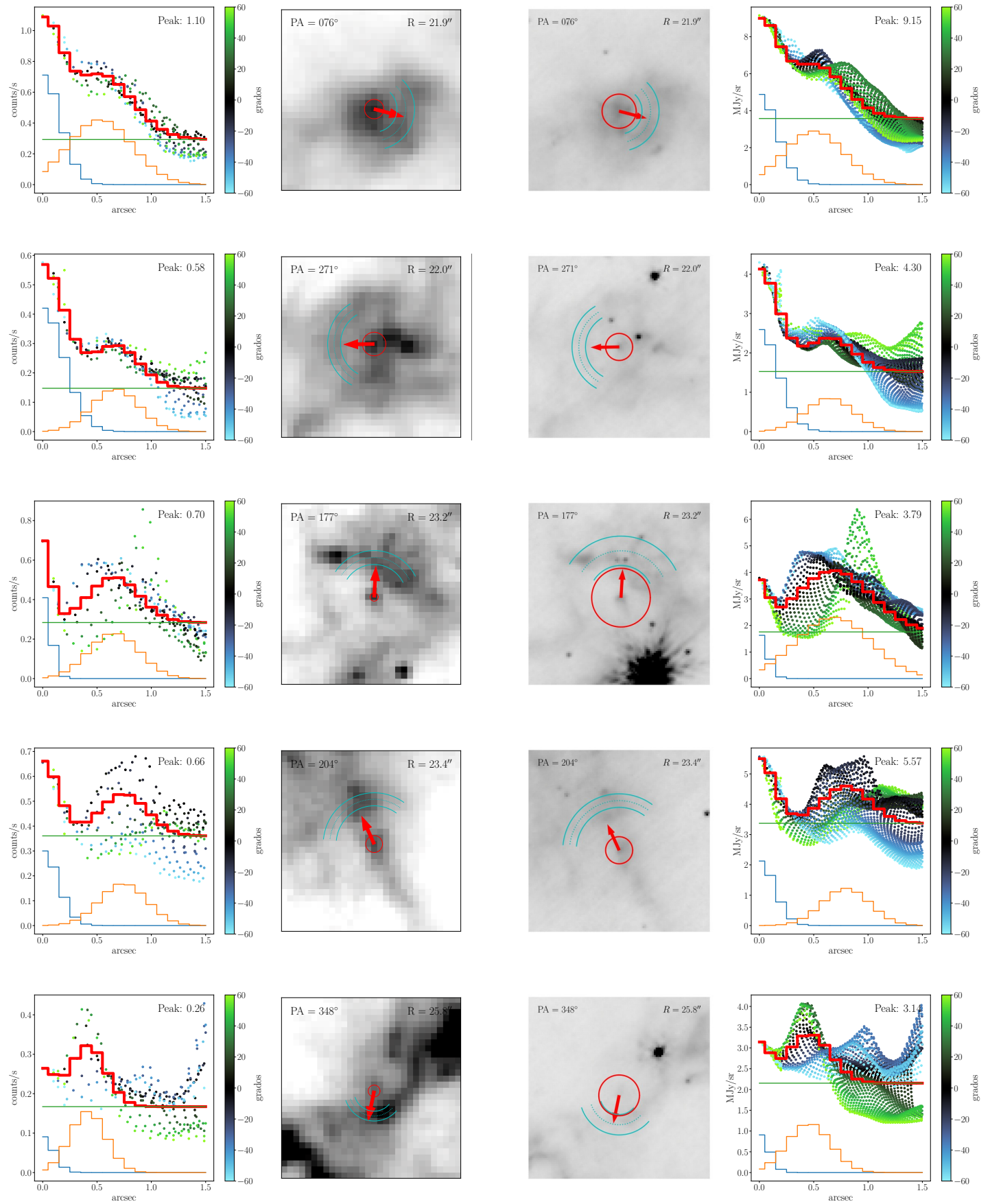


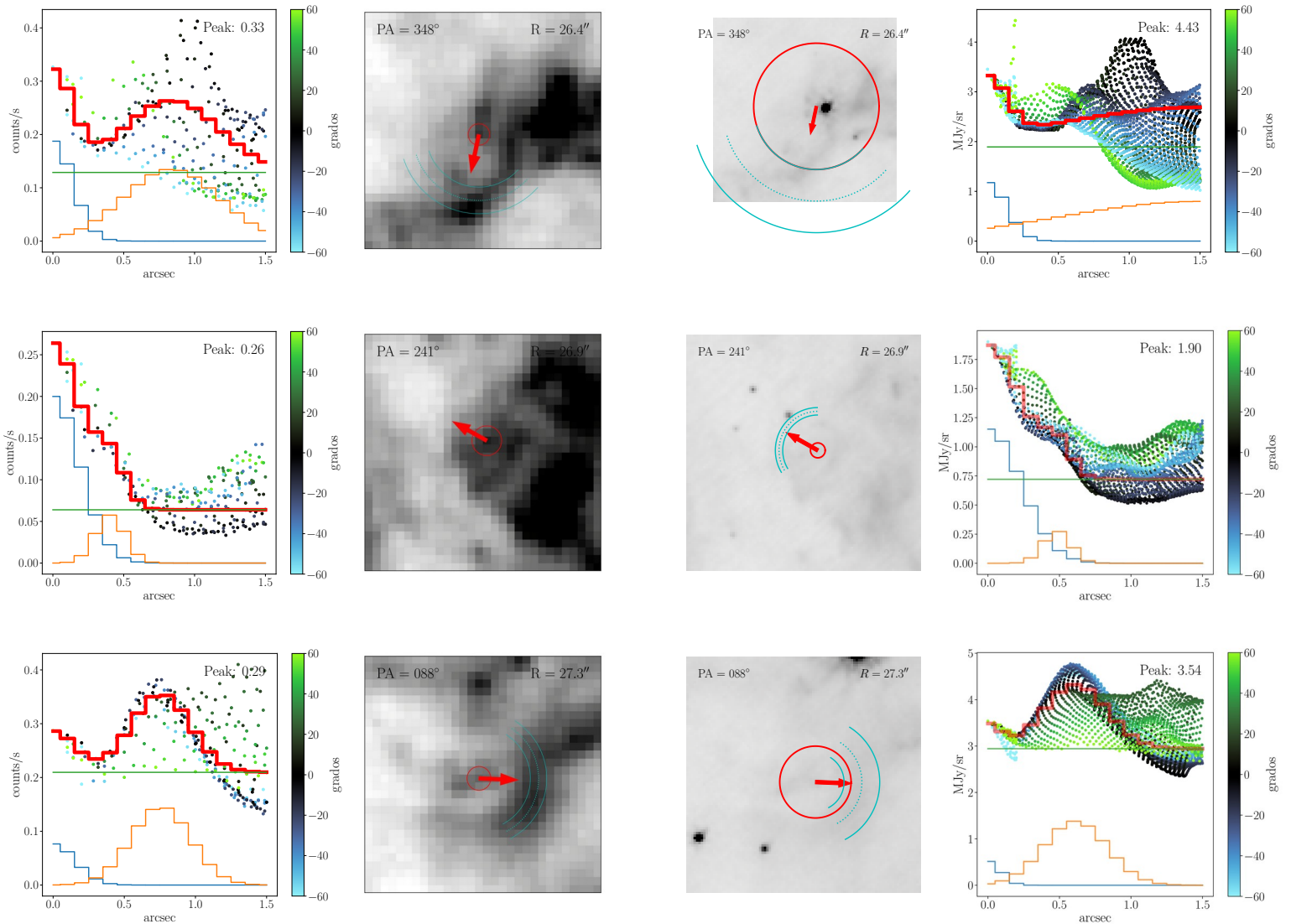
## APPENDIX J. IMÁGENES DE AJUSTES





## APPENDIX J. IMÁGENES DE AJUSTES







# Bibliography

- Alves, J. F., Lada, C. J., & Lada, E. A. 2001, *Nature*, 409, 159
- Amin, M. Y., & El-Nawawy, M. S. 2005, *New A*, 11, 138, doi: [10.1016/j.newast.2005.06.006](https://doi.org/10.1016/j.newast.2005.06.006)
- Ballesteros-Paredes, J., Vázquez-Semadeni, E., Gazol, A., et al. 2011, *MNRAS*, 416, 1436, doi: [10.1111/j.1365-2966.2011.19141.x](https://doi.org/10.1111/j.1365-2966.2011.19141.x)
- Bertoldi, F. 1989, *ApJ*, 346, 735, doi: [10.1086/168055](https://doi.org/10.1086/168055)
- Cantó, J., Raga, A. C., & Wilkin, F. P. 1996, *ApJ*, 469, 729, doi: [10.1086/177820](https://doi.org/10.1086/177820)
- Crowther, P. A. 2007, *ARA&A*, 45, 177, doi: [10.1146/annurev.astro.45.051806.110615](https://doi.org/10.1146/annurev.astro.45.051806.110615)
- Crowther, P. A., Pasquali, A., De Marco, O., et al. 1999, *A&A*, 350, 1007, doi: [10.48550/arXiv.astro-ph/9908200](https://arxiv.org/abs/astro-ph/9908200)
- Di Francesco, J., Hogerheijde, M. R., Welch, W. J., & Bergin, E. A. 2002, *AJ*, 124, 2749, doi: [10.1086/344078](https://doi.org/10.1086/344078)
- Dyson, J. E. 1968, *Ap&SS*, 1, 388, doi: [10.1007/BF00656009](https://doi.org/10.1007/BF00656009)
- Dyson, J. E., & Williams, D. A. 1980, Physics of the interstellar medium
- Gahm, G. F., Persson, C. M., Mäkelä, M. M., & Haikala, L. K. 2013, *A&A*, 555, A57, doi: [10.1051/0004-6361/201321547](https://doi.org/10.1051/0004-6361/201321547)
- García-Arredondo, F., Henney, W. J., & Arthur, S. J. 2001, *ApJ*, 561, 830, doi: [10.1086/323367](https://doi.org/10.1086/323367)
- Grosdidier, Y., Moffat, A. F. J., Joncas, G., & Acker, A. 1998, *ApJ*, 506, L127, doi: [10.1086/311647](https://doi.org/10.1086/311647)
- Hamann, W. R., Gräfener, G., & Liermann, A. 2006, *A&A*, 457, 1015, doi: [10.1051/0004-6361:20065052](https://doi.org/10.1051/0004-6361:20065052)
- Hamann, W.-R., Gräfener, G., Liermann, A., et al. 2019, *A&A*, 625, A57, doi: [10.1051/0004-6361/201834850](https://doi.org/10.1051/0004-6361/201834850)

- Hartigan, P., Reiter, M., Smith, N., & Bally, J. 2015, AJ, 149, 101, doi: 10.1088/0004-6256/149/3/101
- Henney, W. J., & Arthur, S. J. 2019, MNRAS, 486, 3423, doi: 10.1093/mnras/stz1043
- Henney, W. J., Arthur, S. J., de Colle, F., & Mellemma, G. 2009, MNRAS, 398, 157, doi: 10.1111/j.1365-2966.2009.15153.x
- Hester, J. J., Scowen, P. A., Sankrit, R., et al. 1996, AJ, 111, 2349, doi: 10.1086/117968
- Jiménez-Hernández, P., Arthur, S. J., & Toalá, J. A. 2020, MNRAS, 497, 4128, doi: 10.1093/mnras/staa2272
- Marchenko, S. V., Moffat, A. F. J., & Crowther, P. A. 2010, ApJ, 724, L90, doi: 10.1088/2041-8205/724/1/L90
- Mesa-Delgado, A., Zapata, L., Henney, W. J., Puzia, T. H., & Tsamis, Y. G. 2016, ApJ, 825, L16, doi: 10.3847/2041-8205/825/1/L16
- Murdin, P. 2000, in Encyclopedia of Astronomy and Astrophysics, ed. P. Murdin, 4101, doi: 10.1888/0333750888/4101
- O'Dell, C. R., Henney, W. J., & Ferland, G. J. 2007, AJ, 133, 2343, doi: 10.1086/513011
- Oort, J. H., & Spitzer, Lyman, J. 1955, ApJ, 121, 6, doi: 10.1086/145958
- Padoan, P., & Nordlund, Å. 2002, ApJ, 576, 870, doi: 10.1086/341790
- Reiter, M., McLeod, A. F., Klaassen, P. D., et al. 2019, MNRAS, 490, 2056, doi: 10.1093/mnras/stz2752
- Schneider, N., Bontemps, S., Motte, F., et al. 2016, A&A, 591, A40, doi: 10.1051/0004-6361/201628328
- Sévigny, M., St-Louis, N., Drissen, L., & Martin, T. 2021, MNRAS, 501, 5350, doi: 10.1093/mnras/staa3971
- Shu, F. H. 1992, The physics of astrophysics. Volume II: Gas dynamics.
- Smith, L. F., Shara, M. M., & Moffat, A. F. J. 1996, MNRAS, 281, 163, doi: 10.1093/mnras/281.1.163
- Tarango-Yong, J. A., & Henney, W. J. 2018, MNRAS, 477, 2431, doi: 10.1093/mnras/sty669
- van der Hucht, K. A. 2001, New A Rev., 45, 135, doi: 10.1016/S1387-6473(00)00112-3
- Zavala, S., Toalá, J. A., Santamaría, E., et al. 2022, MNRAS, 513, 3317, doi: 10.1093/mnras/stac1097